symmetry

MDPI

Review

Topological Excitations in Neutral–Ionic Transition Systems

Keishi Sunami [1,*,†], Ryosuke Takehara [1,‡], Kazuya Miyagawa [1], Hiroshi Okamoto [2] and Kazushi Kanoda [1,*]

[1] Department of Applied Physics, University of Tokyo, Bunkyo-ku, Tokyo 113-8656, Japan; takehara.r.ab@m.titech.ac.jp (R.T.); kazuya@ap.t.u-tokyo.ac.jp (K.M.)
[2] Department of Advanced Materials Science, University of Tokyo, Kashiwa, Chiba 277-8561, Japan; okamotoh@k.u-tokyo.ac.jp
* Correspondence: k.sunami@aist.go.jp (K.S.); kanoda@ap.t.u-tokyo.ac.jp (K.K.)
† Current address: Research Institute for Advanced Electronics and Photonics, National Institute of Advanced Industrial Science and Technology (AIST), Tsukuba, Ibaraki 305-8565, Japan.
‡ Current address: Laboratory for Chemistry and Life Science, Institute of Innovative Research, Tokyo Institute of Technology, Yokohama, Kanagawa 226-8503, Japan.

Abstract: The existence and physical properties of topological excitations in ferroelectrics, especially mobile topological boundaries in one dimension, are of profound interest. Notably, topological excitations emerging in association with the neutral–ionic (NI) phase transition are theoretically suggested to carry fractional charges and cause anomalous charge transport. In recent years, we experimentally demonstrated mobile topological excitations in a quasi-one-dimensional (1D) ferroelectric, tetrathiafulvalene-*p*-chloranil [TTF-CA; TTF ($C_6H_4S_4$) and CA ($C_6Cl_4O_2$)], which shows the NI transition, using NMR, NQR, and electrical resistivity measurements. Thermally activated topological excitations carry charges and spins in the NI crossover region and in the ionic phase with a dimer liquid. Moreover, free solitons show a binding transition upon a space-inversion symmetry-breaking ferroelectric order. In this article, we review the recent progress in the study of mobile topological excitations emerging in TTF-CA, along with earlier reports that intensively studied these phenomena, aiming to provide the foundations of the physics of electrical conductivity and magnetism carried by topological excitations in the 1D ferroelectric.

Keywords: topological excitation; domain wall; soliton; neutral–ionic transition; electronic ferroelectric

Citation: Sunami, K.; Takehara, R.; Miyagawa, K.; Okamoto, H.; Kanoda, K. Topological Excitations in Neutral–Ionic Transition Systems. *Symmetry* **2022**, *14*, 925. https://doi.org/10.3390/sym14050925

Academic Editors: Serguei Brazovskii and Natasha Kirova

Received: 28 February 2022
Accepted: 26 April 2022
Published: 1 May 2022

1. Introduction

The concept of topology has opened a new window in condensed matter physics for identifying novel electronic states and phenomena [1–6]. Among them, boundaries dividing topologically different phases, such as surfaces for three-dimensional (3D) systems and edges for two-dimensional systems, are intensively researched fields, where peculiar electronic states emerge, such as gapless surface bands [6]. In the studies to date, however, the topological boundaries are built-in systems and remain static. If the topological boundaries are mobile, they are expected to offer new degrees of freedom and open a new phase in the development of topological condensed matter physics. In one-dimensional (1D) systems, the boundaries are in the form of zero-dimensional (0D) points, which can be regarded as a kind of particle and therefore have the potential to be mobile, unlike surfaces and lines in higher dimensions. The representative example of topological excitation in 1D systems is a soliton emerging in a conducting polymer, polyacetylene, in which the charged solitons are responsible for high electrical conductivity [3].

Interestingly, the 1D electronic ferroelectric, in which charge, spin, and lattice degrees of freedom are strongly entangled, is suggested to host the solitons as elementary excitations carrying a fractional charge and unusual conducting properties. The neutral–ionic (NI) transition material tetrathiafulvalene-*p*-chloranil (TTF-CA), which is a quasi-1D

ferroelectric, has long been argued to be a promising candidate for the emergence of such topological excitations [7–15]; however, the existence and physical properties of thermally excited solitons as suggested theoretically remain elusive. Recently, experimental studies on topological excitations in the NI transition system have made remarkable progress because the phase diagram, revisited with experiments performed in a regime with higher pressure than ever, has proved to have features that can host topological excitations at high temperatures [16–19]; more specifically, the mobile topological spin and charge excitations, namely, spin solitons and the neutral–ionic domain wall (NIDW), are captured by nuclear magnetic resonance (NMR) and electrical resistivity measurements. Such excitations lead to a novel mechanism of electrical conduction. Moreover, the solitons show a binding transition upon the long-range ferroelectric order, which is a unique phenomenon that has never been observed in conducting polymers.

In this review article, we report the recent progress in the physics of mobile topological excitations in TTF-CA. In Section 2, we briefly introduce the fundamental properties of the NI transition material TTF-CA and the concept of topological excitations emerging in this system. In Section 3, we describe the pressure–temperature (*P*-*T*) phase diagram of TTF-CA revisited by nuclear quadrupole resonance (NQR) and highlight high-temperature characteristics revised from an earlier report. In Section 4, we review the experimental studies on electrical conductivity and magnetism brought about by mobile topological excitations in TTF-CA; the paramagnetism carried by mobile spin solitons (Section 4.1); the anomalous charge transport caused by mobile NIDWs and solitons (Section 4.2); and the binding transition of solitons upon the space-inversion symmetry-breaking ferroelectric order (Section 4.3). In Section 5, we summarize this review.

2. Topological Excitations in Neutral–Ionic Transition Systems

2.1. Neutral–Ionic Transition Material TTF-CA

The quasi 1D donor–acceptor (DA) complex, TTF-CA, is a strongly charge–spin–lattice coupled system, which is the representative NI transition material [20–30]. Molecular arrangements in TTF-CA are shown in Figure 1a,b. The TTF and CA molecules alternatingly stack face-to-face along the *a*-axis, forming 1D chains. At ambient temperature and pressure, TTF-CA is in a quasi-neutral (N) state; the highest occupied molecular orbitals (HOMOs) of the donor molecule, TTF, and the acceptor molecule, CA, are doubly occupied by electrons. Upon cooling, the system transitions to a quasi-ionic (I) state at 81 K with an electron transfer from the HOMO of TTF to the lowest unoccupied molecular orbital (LUMO) of CA due to the Madelung energy gain (see Figure 2) [21,23]. The Madelung energy incorporates long-range Coulomb interactions between all of the molecules in the crystal, and thus, the charge transfer upon the NI transition is a collective phenomenon. The N and I phases are characterized by the degree of charge transfer ϱ defined by $D^{+\varrho}A^{-\varrho}$: $\varrho_N \sim 0.3$ in the N phase and $\varrho_I \sim 0.6$–0.7 in the I phase [24,31–35]. The partial charge transfer from TTF to CA is due to the hybridization of the molecular orbitals between them.

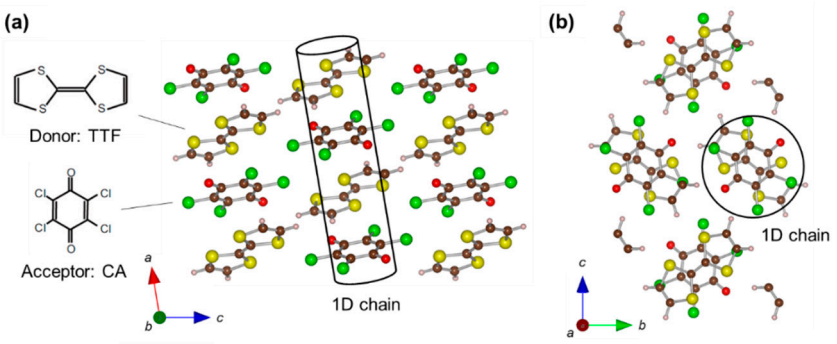

Figure 1. Molecular arrangements in the *ac* plane (**a**) and *bc* plane (**b**) in the neutral phase of TTF-CA.

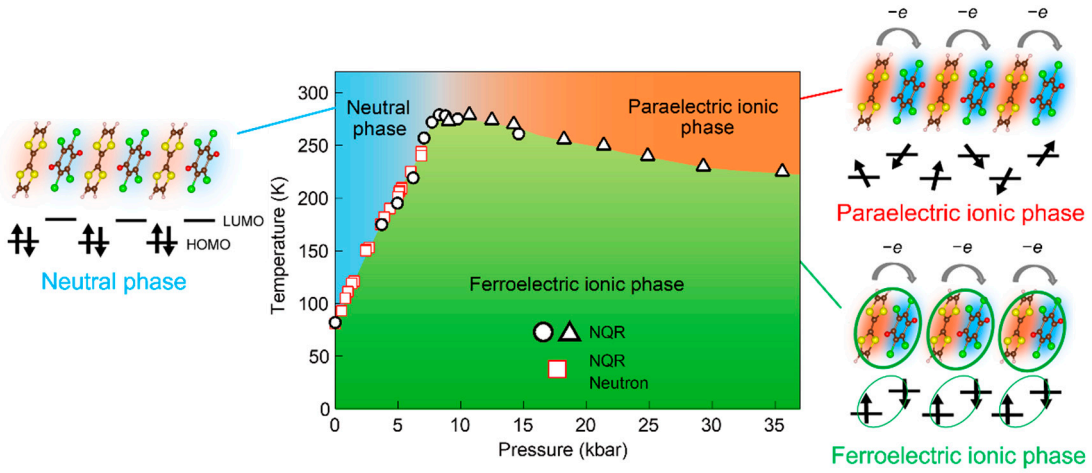

Figure 2. Pressure–temperature phase diagram of TTF-CA. Black open circles (sample #1) and triangles (sample #2) represent the phase transition temperatures T_c determined by the NQR experiments in [16]. Red open squares represent T_c determined by the NQR and neutron experiments in [36]. Reprinted with permission from [16]. Copyright 2018, American Physical Society. Schematics in the sides of the central panel depict the electron configurations in space and energy in TTF and CA molecules; red and blue clouds represent the hole and electron densities in HOMO of TTF and LUMO of CA by color intensity. Reprinted with permission from [18]. Copyright 2019, The Authors, some rights reserved; exclusive licensee AAAS. Distributed under a CC BY-NC 4.0 License (http://creativecommons.org/licenses/by-nc/4.0/(accessed on 15 November 2021)).

Lattice dimerization is caused in the charge-transferred I phase due to the Peierls or spin-Peierls instability inherent in 1D systems [25,37–39]. Thus, the 1D dimerized chains are polarized, which show a long-range ferroelectric order in the I phase. The ferroelectricity in TTF-CA is of keen interest because the charge transfer coupled with the dimerization yields electronic ferroelectricity [40–43], which can be described by a modern ferroelectric theory in the framework of a Berry phase [44–47].

The charge transfer upon the NI transition generates an $S = 1/2$ spin on each molecule in the I phase, but the spins form singlet pairs due to the dimerization. Thus, TTF-CA is a nonmagnetic insulator in both the N phase and ionic ferroelectric (I_{ferro}) phase at ambient pressure: a band insulator with a closed-shell structure in the former phase and an ionic Mott insulator with a spin-singlet formation in the latter phase. In the following sections, we review studies showing that the entanglement of charge, spin, and lattice degrees of freedom brings about emergent excitations with topological character in TTF-CA.

2.2. Types of Topological Excitations in Neutral–Ionic Transition Systems

The concept of topological excitations in the NI transition systems was theoretically proposed in the 1980s [7,48,49] as defects that emerge in between domains of degenerate ground states and thus are activated near the region where more than two phases compete. In the NI transition system of TTF-CA, the N and I_{ferro} phases are degenerate near the NI phase boundary due to the coupling between charge-transfer and lattice instabilities, as mentioned in Section 2.1. Moreover, two opposite polar patterns (denoted by I_A and I_B in Figure 3) are degenerate in the I_{ferro} phase. Thus, it is theoretically proposed that neutral–ionic domain walls (NIDWs) reside in between the N and I_A (or I_B) domains, and spin and spinless solitons are located in between the I_A and I_B domains (see Figure 3). The spinless soliton is often called a charge soliton, which corresponds to a single neutral molecule sandwiched by two NIDWs. The difference between spin and charge solitons comes from the number of electrons that occupy the molecular orbital of the soliton site; for the spin soliton, the HOMO of D or the LUMO of A is occupied by one electron, whereas, for the charge soliton, the HOMO of D is fully occupied or the LUMO of A is empty. The topological nature of these excitations is expressed based on the phase Hamiltonian in [7,10].

Physically, phases of charge, spin, and lattice modulations have discontinuities at the NI domain walls, spin solitons, and charge solitons; these discontinuities that are characterized by topological charge or spin are robust and cannot annihilate without pair collision. These excitations have fractional charges: $e(\varrho_I - \varrho_N)/2$ for the NIDW, $e(1 - \varrho_I)$ for the spin soliton, and $-e\varrho_I$ for the charge soliton, where e is the elementary charge. Remarkably, the NIDW is freely mobile near the NI boundary where the N and I states are degenerate, and its excitation energy is lowered due to the itinerant nature, attributed to the large transfer integral along the 1D direction [48]. Thus, NIDWs can be low-energy excitations in NI transition systems uniquely and are expected to yield unconventional charge transport that differs from that of individual electrons, as theoretically suggested [7,9,10]; note that both the NIDW (or charge soliton) and spin soliton are necessary for carrying a steady electrical current, the mechanism of which is briefly explained in Section 4.2.

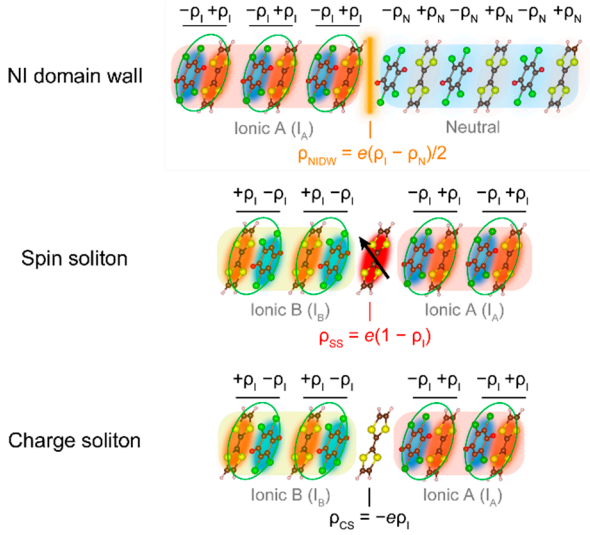

Figure 3. Topological excitations in neutral–ionic phase transition systems. ϱ_{NIDW}, ϱ_{SS}, and ϱ_{CS} are topological charges of a NI domain wall, a spin soliton, and a charge soliton, respectively. ϱ_N and ϱ_I represent the degree of charge transfer from HOMO of TTF and LUMO of CA in the neutral and ionic phases, respectively. Modified with permission from [18]. Copyright 2019, The Authors, some rights reserved; exclusive licensee AAAS. Distributed under a CC BY-NC 4.0 License (http://creativecommons.org/licenses/by-nc/4.0/(accessed on 15 November 2021)).

In the past, these topological boundaries were observed as frozen defects in the ferroelectric phase and its vicinity. The spin solitons were detected in the I_{ferro} phase at ambient pressure by ESR measurements [11,50], which were generated in the multi-domain structure of the I_{ferro} phase (the typical ferroelectric domain size was reported to be ~100 μm [51]) when cooled below the transition temperature T_c. Thus, they behave as frozen defects, not thermally activated, in the 3D ferroelectric order. The density of the thus-generated spin soliton was estimated to be ~10^{-4} spins per molecule from the absolute value of spin susceptibility, which is extremely dilute. The emergence of charge solitons was suggested by dielectric measurements [15,50], which found an anomalous enhancement of the dielectric constant in the I_{ferro} phases with a characteristic frequency dependence in a frequency range below ~MHz. It was attributed to the motions of charge solitons. Enhanced dielectric constants in an analogous material, TTF-$QBrCl_3$, are suppressed by electric-field poling, which varies the density of frozen charge solitons in the ferroelectric phase [50], indicating the involvement of domain boundaries in enhanced dielectric constants.

In the N phase near the NI transition temperature, fluctuating I domains sandwiched by two NIDWs with charges of opposite signs were detected [52,53]. Their motion is suggested to contribute to the enhancement of dielectric constants in the N phase [15], as with the charge solitons in the I_{ferro} phase. Moreover, the NIDW motion also pertains to the

photoinduced phase transition (PIPT) of TTF-CA, which has long attracted much attention as a prototypical system of PIPT [29,54–58]. The N and I phases can be switched by photoirradiation; recent studies have shown that the electric polarization is controllable using the THz electric-field pulse, causing the displacement of the NIDW [53,59].

Regarding the charge transport, intriguing phenomena have been observed [12,14]; the two-terminal resistivity decreases around the NI transition under ambient pressure in TTF-CA despite the fact that the system is an insulator in both the N and I_{ferro} phases, which evokes some unconventional conduction mechanism. However, this decrease is not due to the NIDW or soliton conduction, as was demonstrated by resistivity measurements under the electric-field control of the soliton density in the TTF-$QBrCl_3$ mentioned above [50]; the electrical conductivity increases when the soliton density is suppressed, possibly suggesting that the soliton is the carrier scatterer, rather than the charge carrier.

Why has the topological charge transport been experimentally elusive in the NI transition system? This is very probably because the 3D long-range ferroelectric order prohibits the travel of NIDWs and solitons at ambient pressure (although the displacement current flows due to their transient motions). Thus, if NIDWs are activated in the nonordered paraelectric regime, they may travel and carry a charge current. As reported in Sections 3 and 4, we demonstrated anomalous charge transport by topological excitations under pressures where the N phase and the I phase free from the dimer order, which we call the paraelectric ionic (I_{para}) phase, are temporally fluctuating. Moreover, in the 3D ferroelectric ordered (I_{ferro}) phase, instead of frozen solitons, we revealed that bound pairs of solitons are responsible for charge and spin excitations.

3. Revisited Pressure–Temperature Phase Diagram of TTF-CA

3.1. Previous Phase Diagram

In this section, we describe the physical properties of TTF-CA under pressure. First, we summarize under-pressure studies conducted earlier in TTF-CA using neutron scattering, X-ray diffraction, NQR, optical spectroscopy (using infrared and visible light), dielectric, and electrical conductivity measurements [22,36,60–62]. The NI transition occurs simultaneously with the dimerization transition under pressures of up to ~7 kbar, as detected by NQR and neutron scattering measurements (Figure 2); with increasing pressure, the phase transition temperature, T_c, shows a continuous increase, and the jump in the degree of charge transfer ϱ is diminished. Upon a pressure sweep at room temperature, DA dimerization is detected at high pressures by infrared spectroscopy measurements, which show that the intensity of the a_g mode of the CA molecule, which is sensitive to DA dimerization, is rapidly enhanced above 8 kbar and reaches a maximum at 11 kbar [27,63,64]. X-ray scattering showed an anomalous lattice-parameter change in the *a*-axis direction at pressures of 6.5–11 kbar at 300 K that deviated from the pressure evolution in the lattice parameter in the N and I phases [62]; thus, a ferroelectric transition at 11 kbar was inferred. The electrical conductivity measured by the two-terminal method exponentially increases with pressure and exhibits a peak at ~9 kbar [12,14], which is almost located on the extrapolation of the NI transition line determined by NQR and neutron scattering at lower pressures below 7 kbar. Thus, the inclined NI transition line between the N and I_{ferro} phases is likely to be in the *P*-*T* phase diagram.

On the other hand, the temperature profiles of NQR and neutron diffraction data near 7 kbar suggest that the charge transfer may be separated in temperature from that of the symmetry-breaking dimerization transition [22,36]. In addition, the dielectric constant exhibits two-step changes upon cooling at pressures $P < 9$ kbar coincidentally at the temperatures of the charge transfer and the lattice symmetry breaking determined by the neutron and NQR measurements. These features signify that some change occurs in the system prior to the long-range dimer order; possibly, the charge-transfer transition line is separated from the dimerization transition line on the phase diagram. This bifurcation indicates the existence of a non-dimerized paraelectric ionic (I_{para}) phase between the two

lines (charge transfer and dimer order). We note that the above-mentioned a_g-mode activation does not necessarily entail the long-range order of dimerization, as discussed later. Moreover, it was predicted that the charge-transfer transition line has a critical endpoint because the charge transfer transition itself is not accompanied by lattice symmetry breaking [22,36,61,65]. As mentioned in Section 2.2, if the I_{para} phase is stabilized, there appears to be room for the emergence of topological charge transport, which is immobile in the 3D ferroelectric dimer order, in the vicinity of the boundary between the N and I_{para} phases. However, experiments with varying temperatures were only limited to below 9 kbar [22,36,60]. Thus, further investigations at higher pressures are awaited.

3.2. Revisited Phase Diagram: Ionic Paraelectric Phase Hosting Dimer-Liquid State

To clarify the existence of the I_{para} phase, we conducted a ^{35}Cl-NQR measurement, which is a microscopic probe of the charge and lattice states, on the polycrystalline TTF-CA under zero magnetic field in an extended pressure range up to 35 kbar [16]. We used Daphne 7373 (for $P < 20$ kbar) and 7474 (for $20 < P < 35$ kbar) oils as the pressure media. The NQR frequency is proportional to the electric-field gradient at the ^{35}Cl nuclear position in a CA molecule, which is determined by the local charge distribution. As demonstrated by earlier NQR experiments, the charge transfer and lattice dimerization are directly signified by the profile of NQR lines [22,36,66,67]; the charge transfer is captured by the shift of the center of gravity of the lines due to the change in the molecular charge, and the lattice dimerization is indicated by line splitting due to the loss of the inversion center on the CA molecule.

At ambient pressure, we observed two ^{35}Cl NQR spectra above T_c, arising from the two inequivalent Cl sites in each CA molecule (all of the CA molecules are crystallographically equivalent in the N phase [37]). Because both spectra show similar behaviors in response to temperature variation, we investigated the NQR line residing on the higher-frequency side. Upon cooling at ambient pressure, a single ^{35}Cl NQR line observed in the N phase splits into two lines below $T_c = 82$ K, accompanied by a jump in the center of gravity of the spectra (see Figure 4a). This indicates that the charge transfer and the dimerization coincide at ambient pressure, as earlier results indicated [66,67]. With increasing pressure at room temperature, however, the NQR line shows a pronounced shift at ~9 kbar but no line splitting up to 35 kbar (see Figure 4b), suggesting that a sharp charge transfer without static lattice dimerization occurs at ~9 kbar. Moreover, upon cooling at a high pressure of 18.2 kbar, we observed a clear line splitting below 258 K, which was not accompanied by an apparent change in the center of gravity of the split lines, as shown in Figure 4c. These results demonstrate that the non-dimerized ionic paraelectric (I_{para}) phase emerges at high temperatures and pressures due to decoupling between the charge transfer and dimer order. The NQR experiments show that, above 8.5 kbar, the dimerization transition temperature (corresponding to the I_{para}-to-I_{ferro} transition temperature) decreases with pressure (see Figure 4d); the I_{para} phase is extended up to 35 kbar, as depicted in Figure 2.

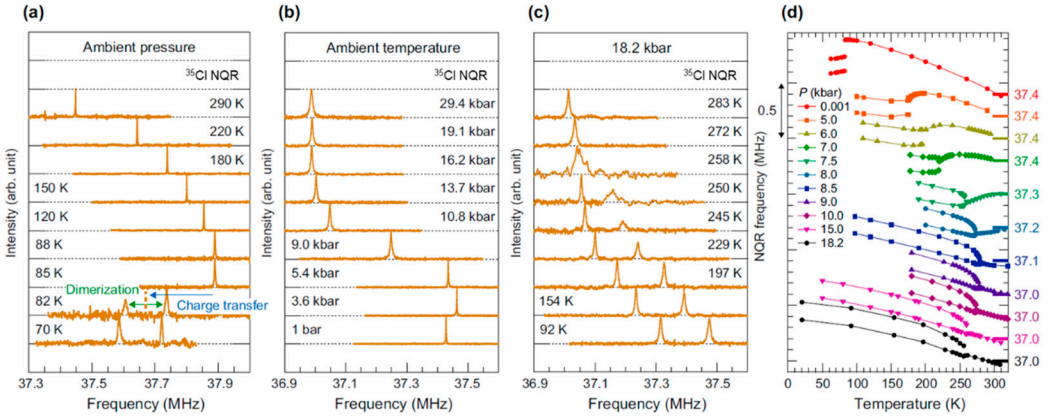

Figure 4. (**a**–**c**) Temperature and pressure profiles of the ^{35}Cl-NQR spectra. (**d**) Temperature dependence of the ^{35}Cl-NQR frequencies at fixed pressures. Reprinted with permission from [16]. Copyright 2018, American Physical Society.

To discuss the profiles of the charge transfer in more detail, we converted the center of gravity of NQR frequency ν_Q (Figure 5a) to the degree of charge transfer ρ using the optical data for reference [33,34]. The details of the estimation of ρ are given in [16]. Here, the main points are briefly summarized below. We assumed that (i) the temperature dependence of ν_Q in the state of $\rho = 0$ obeys the Koukoulas function, which is a well-known formula empirically describing the lattice vibration effect on ν_Q [68] (Figure 6a), (ii) ν_Q depends linearly on ρ at a given temperature (Figure 6a), and (iii) the pressure effect on ν_Q is corrected using the ν_Q data in the neutral CA crystal with $\rho = 0$ (Figure 6b). Based on these assumptions, the relationship between ν_Q and ρ is expressed as $\nu_Q(P, T) = \nu_0\exp(-\alpha T^2) + A\rho(P, T) + a[1 - \exp(-bP)]$, where A, ν_0, α, a, and b are constants independent of temperature and pressure. The three terms express the three assumptions, respectively. The ρ value estimated using the above formula increases with the application of pressure or decreasing temperature, as shown in Figure 5c, and the jump in ρ at T_c is diminished with increasing pressure up to 7 kbar and becomes quite small at higher pressures (Figure 5d). This appears to be linked to the jump in the line splitting width at T_c, which also decreases with pressure (Figure 5b). These behaviors signify that the NI transition accompanied by the dimer order becomes second-order at high pressures, consistent with previous reports [22,36]. Above 7 kbar, where the charge transfer and dimer order are less coupled, the change in ρ at T_c is nearly zero or takes a negative value, possibly implying that the charge is backflowed by the promotion of molecular orbital hybridization due to dimerization, as suggested in a theoretical study [7].

Is the change from the N to I_{para} phase a phase transition or a crossover? Does the critical endpoint of charge transfer exist? To answer these questions, we plotted the detailed pressure dependence of ρ at fixed temperatures in Figure 5e. The ρ value exhibits a sharp but continuous change around 8 kbar at 280–320 K. There was no discontinuous anomaly in ρ on the boundary between the N and I_{para} phases, indicating that the charge transfer occurs as a crossover. For the critical endpoint of the charge transfer suggested by previous works [22,36,61], it was not captured at least by our experiments. These behaviors are summarized in Figure 5f as the contour plot of ρ on the P-T phase diagram along with the dimerization transition temperature, represented by the white line. This figure clearly indicates that the charge transfer is separated from the dimer order above ~8 kbar, and the charge-transfer crossover line is an extension of the NI transition line determined at pressures below ~7 kbar. Note that the slight jump in ρ at ~7 kbar under 240–260 K in Figure 5e is an indication of the weak first-order N-to-I_{ferro} transition, not the change from the N to I_{para} phase (see Figure 5f).

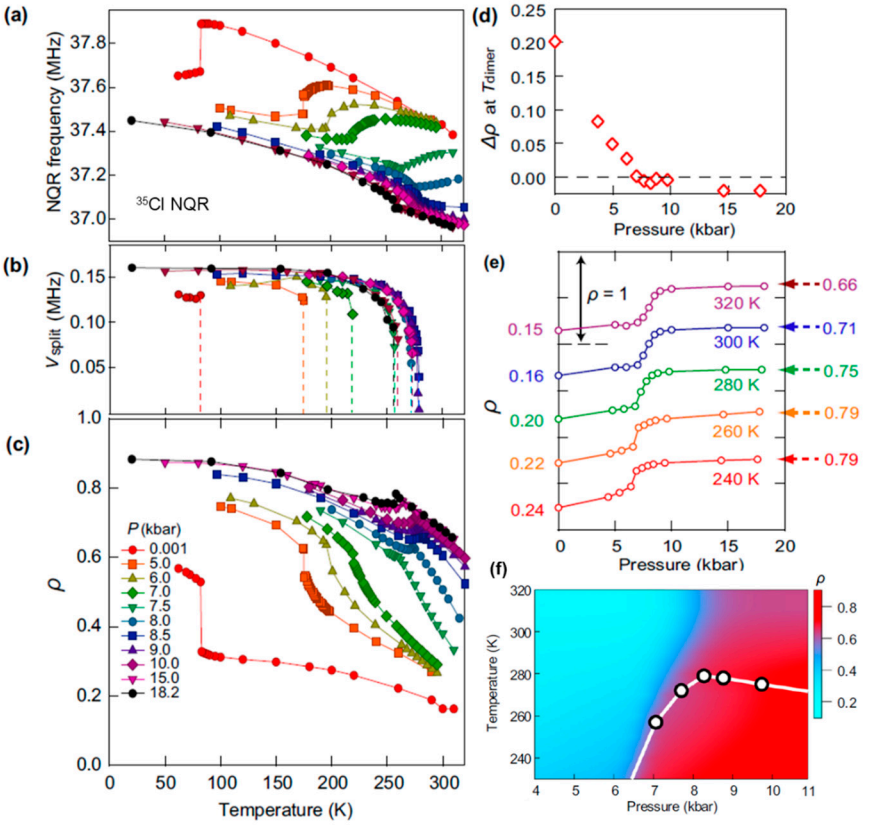

Figure 5. Temperature dependence of the center of gravity of ^{35}Cl-NQR frequency (**a**), line splitting width (**b**), and the degree of charge transfer ϱ evaluated from the ^{35}Cl-NQR frequency (**c**) under various pressures. (**d**) The jump in ϱ, Δϱ, at the dimerization temperature. (**e**) Pressure profiles of ϱ at fixed temperatures. (**f**) The contour plot of ϱ in the pressure–temperature phase diagram. Open circles represent the phase transition temperatures T_c determined by the NQR experiments, corresponding to those in Figure 2. Reprinted with permission from [16]. Copyright 2018, American Physical Society.

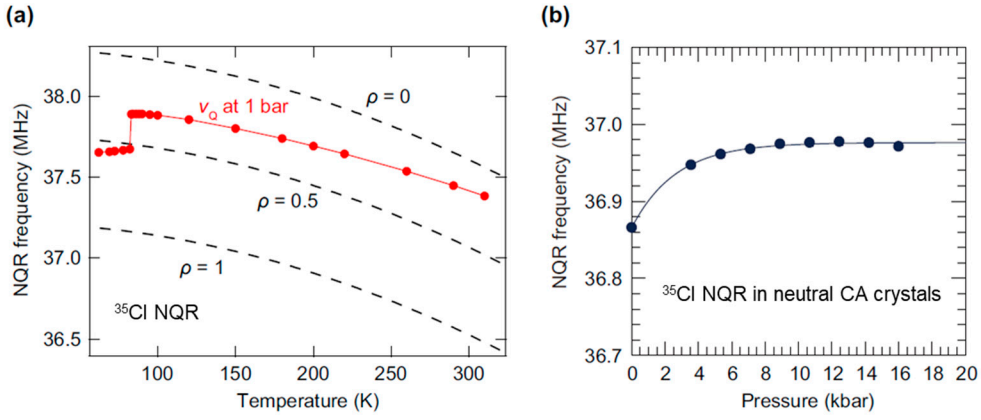

Figure 6. (**a**) Relationship between the ^{35}Cl-NQR frequency ν_Q and the degree of charge transfer ϱ at ambient pressure. Red circles are the experimental ν_Q values at 1 bar and red line is a guide for the eye. Broken lines are the calculated temperature dependence of ν_Q in the state of ϱ = 0, 0.5, and 1, expressed by the Koukoulas function. (**b**) Pressure dependence of the ^{35}Cl-NQR frequency in neutral CA crystals at room temperature. The line is a fit of $a[1 - \exp(-bP)]$ to the data (see text and [16] for details). Reprinted with permission from [16]. Copyright 2018, American Physical Society.

The emergence of the I_{para} phase in the high-temperature and -pressure region appears to be incompatible with the observation of active a_g mode related to the dimerization

by infrared spectroscopy above 8 kbar [27,63,64]. This discrepancy can be resolved by the picture that the I_{para} phase is in a liquid state of DA dimers, which are temporally fluctuating at a rate in between the two time scales of the experimental probes, ~10^{-7} s in NQR and ~10^{-12} s in infrared spectroscopy. As further evidence for the dimer liquid, extraordinarily enhanced lattice fluctuations are captured by the ^{35}Cl-NQR relaxation rate $^{35}T_1^{-1}$ (see Figure 7). The $^{35}T_1^{-1}$ value in the I_{para} phase is two orders of magnitude larger than that in the N phase, suggesting that lattice relaxation is caused by the developed dimer fluctuations in the dimer-liquid state. The slight decrease in the ambient temperature $^{35}T_1^{-1}$ with increasing pressures above 10 kbar is possibly related to the decrease in the dimerization transition temperature, which causes a tendency to reduce critical fluctuations at ambient temperature while moving away from the transition temperature at higher pressures.

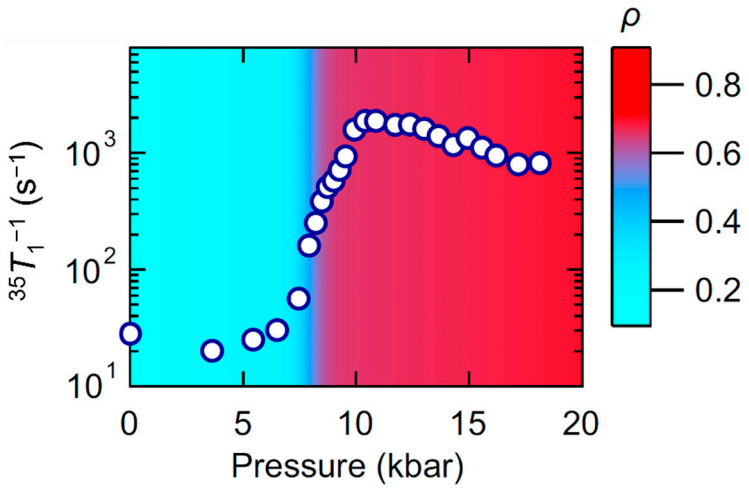

Figure 7. Pressure dependence of the ^{35}Cl-NQR spin–lattice relaxation rate $^{35}T_1^{-1}$ at ambient temperature. The color represents the degree of charge transfer ϱ and corresponds to the color in Figure 5f. Reprinted with permission from [16]. Copyright 2018, American Physical Society.

In the I_{para} phase hosting the dimer-liquid state, the mobile spin solitons are expected to emerge on the boundaries between the fluctuating opposite polar domains. Near the crossover region between the N and I_{para} phases, the separation of the charge transfer from the long-range dimer order may generate mobile NIDWs in 1D chains, which carry electrical currents, as suggested by theoretical studies [7,9,10].

4. Experimental Evidence for Mobile Topological Excitations Emerging in TTF-CA

4.1. Magnetism in the Ionic Paraelectric Phase: Spin Soliton

In this section, we review the results of NMR experiments on spin excitations in TTF-CA [17]; the aim of this study was to demonstrate the emergence of the mobile spin solitons in the I_{para} phase of TTF-CA. Naively, the I_{para} phase should carry paramagnetic spins on uniform 1D chains; however, the fact that the I_{para} phase hosts the dimer-liquid state implies the emergence of mobile solitonic spins at thermally activated topological boundaries separating oppositely polarized dimer domains.

First, we performed NMR experiments for ^{1}H sites in TTF molecules. Figure 8a shows the pressure profiles of the ^{1}H-NMR spin–lattice relaxation rate $^1T_1^{-1}$, probing electron spin fluctuations, at fixed temperatures. At 103 K, where the system shows the N-to-I_{ferro} transition with increasing pressure, $^1T_1^{-1}$ is vanishingly small throughout the N and I_{ferro} phases, indicative of nonmagnetic states, which accords with previous ^{1}H-NMR results [69,70] and is reasonable because of the closed-shell structure for the N phase and spin-singlet pairing for the I_{ferro} phase. Remarkably, at higher temperatures, the $^1T_1^{-1}$ values are enhanced only in the pressure region above the NI crossover. Consistent behaviors are seen in the temperature dependence of $^1T_1^{-1}$ at ambient pressure (the N-to-I_{ferro} transition)

and 13 kbar (the I_{para}-to-I_{ferro} transition), as shown in Figure 8b; $^1T_1^{-1}$ at ambient pressure is vanishingly small over the whole temperature range below 300 K, whereas $^1T_1^{-1}$ at 13 kbar takes large values near room temperature in the I_{para} phase and is drastically suppressed upon entering the I_{ferro} phase. Note that $^1T_1^{-1}$ below T_c at 13 kbar adopts a shoulder structure around 200 K; however, the ^{13}C-NMR relaxation rate, $^{13}T_1^{-1}$, exhibits no such clear shoulder, although there is a sign of it, as shown later. Although the origin of the different behaviors is not clear, the non-monotonous temperature dependence of the relaxation rate is possibly because two types of spin excitations, such as the spin-triplet and the polaron, are responsible for T_1^{-1} in the I_{ferro} phase, as described in Section 4.3; just below T_c, the former, with higher excitation energy, is drastically suppressed upon cooling and almost vanishes around 200 K, whereas the latter, with lower excitation energy, gradually decreases and survives at a lower temperature. The detailed temperature profile of spin excitations upon the I_{para}-to-I_{ferro} transition is discussed in Section 4.3. The contour plot of $^1T_1^{-1}$ depicted on the *P*-*T* plane using these data clearly illustrates that the I_{para} phase is the hot spot of activated spins (see Figure 8c). The kink temperatures of $^1T_1^{-1}$ well coincide with T_c determined by the NQR measurements described in Section 3.2.

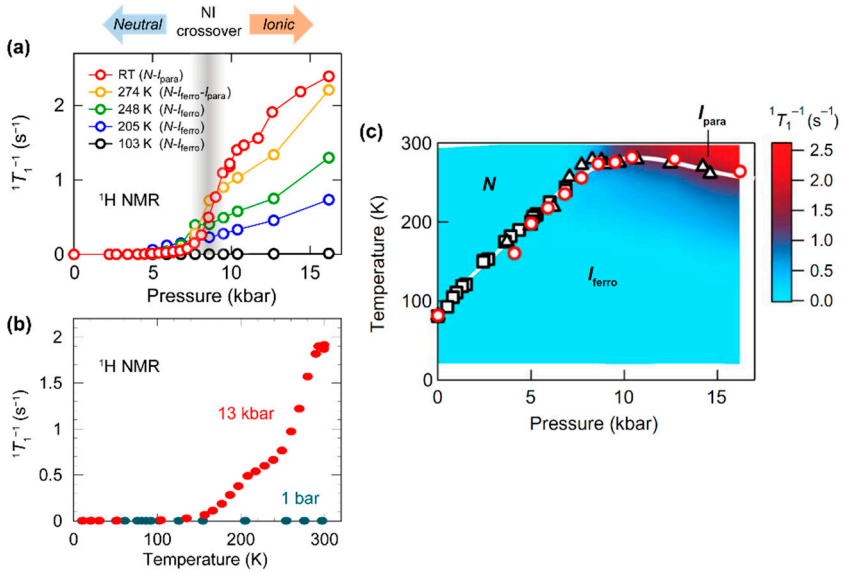

Figure 8. (**a**) Pressure profiles of the ^{1}H-NMR spin–lattice relaxation rate $^1T_1^{-1}$ at fixed temperatures. (**b**) Temperature profiles of $^1T_1^{-1}$ at ambient pressure (blue circles) and 13 kbar (red circles). (**c**) Contour plot of $^1T_1^{-1}$ in the pressure–temperature phase diagram. Red open circles are the phase transition temperatures T_c determined by the kink temperatures of $^1T_1^{-1}$. Black open squares and triangles represent T_c determined by neutron and NQR measurements, respectively [16,36]. Reprinted with permission from [17]. Copyright 2018, The Authors, some rights reserved; exclusive licensee AAAS. Distributed under a CC BY-NC 4.0 License (http://creativecommons.org/licenses/by-nc/4.0/(accessed on 30 November 2021)).

Are these spins activated in the I_{para} phase the mobile spin solitons or alternative spin excitations? To clarify the nature of spin excitations, two experiments were conducted; one is NMR measurement for ^{13}C nuclei on the central double-bonded carbon sites in TTF (Figure 9a), which are more strongly hyperfine-coupled to electron spins than ^{1}H nuclei located on the edges of TTF, and the other is the measurement of the frequency dependence of $^1T_1^{-1}$, which probes the frequency profile of the spin dynamics.

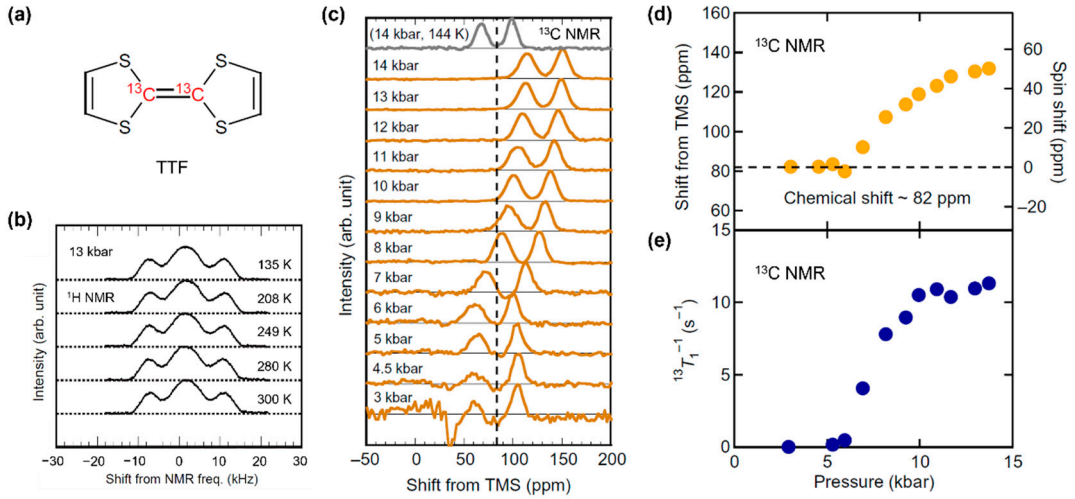

Figure 9. (**a**) ^{13}C-enriched TTF molecule, in which the central double-bonded carbon atoms are substituted by ^{13}C isotopes with a 99% concentration. (**b**) Temperature profile of ^{1}H-NMR spectra at 13 kbar. (**c**) ^{13}C-NMR spectra measured at 285 K under various pressures. The gray spectrum was measured at 14 kbar and 144 K in the ionic ferroelectric phase. The origin of the shift corresponds to the resonance frequency of tetramethylsilane (TMS). Pressure profiles of the ^{13}C-NMR spectral shift (**d**) and spin–lattice relaxation rate $^{13}T_1^{-1}$ (**e**) at 285 K. Reprinted with permission from [17]. Copyright 2018, The Authors, some rights reserved; exclusive licensee AAAS. Distributed under a CC BY-NC 4.0 License (http://creativecommons.org/licenses/by-nc/4.0/(accessed on 30 November 2021)).

In ^{13}C-NMR measurements, the spin susceptibility χ is quantitatively estimated from the NMR spectral shift owing to the strong hyperfine interaction with electron spin. We compare the NMR spectra for the ^{1}H site (Figure 9b) and ^{13}C site (Figure 9c). Each spectrum is composed of multiple peaks due to dipolar interactions between nuclear spins (^{1}H-^{1}H spins for ^{1}H-NMR and ^{13}C-^{13}C spins for ^{13}C-NMR). The ^{13}C-NMR spectrum at 285 K is clearly shifted towards higher frequencies above 7 kbar from its positions in the nonmagnetic N phase at lower pressures or in the nonmagnetic I_{ferro} phase at 14 kbar and 144 K, as shown in Figure 9c. On the other hand, the ^{1}H-NMR spectra at 13 kbar are almost invariant throughout the nonmagnetic I_{para}-to-I_{ferro} transition upon cooling. These indicate that the ^{13}C nuclei are strongly hyperfine-coupled with electron spins, which allows us to evaluate the spin susceptibility. Note that the ^{13}C-NMR spectral shifts observed below 6 kbar of ~82 ppm are attributed to the chemical shift, not contributed to by electron spins, because they fairly well agree with the value observed in the I_{ferro} phase of the nonmagnetic state, represented by the gray line in Figure 9c, which is independent of temperature, as described in Section 4.3.

If the I_{para} phase is not in the dimer-liquid state, the spins should form homogeneous localized spin chains described by the 1D antiferromagnetic Heisenberg model (AFHM). Thus, by comparing the 1D AFHM calculations of χ and the nuclear spin–lattice relaxation rate $^{13}T_1^{-1}$ to the experimental χ and $^{13}T_1^{-1}$ values, we examine whether the present spin state can be described by the 1D AFHM or not. In the I_{para} phase at 14 kbar, the ^{13}C-NMR spin shift, S, proportional to χ, reaches 51 ppm (Figure 9d), and $^{13}T_1^{-1}$ takes a value of 11 s^{-1} (Figure 9e). The spin shift S is expressed as $S = a_{\parallel}\chi/\mu_B N_A$, where N_A is the Avogadro constant, μ_B is the Bohr magneton, and $a_{\parallel}$ is the hyperfine coupling component parallel to the magnetic field H. Through this expression, S is converted to an χ value of 2.6×10^{-5} emu/TTF mol at 14 kbar. Note that we used $^{13}a_{\parallel} = 10.8$ kOe/μ_B of the analogous material, $(TMTTF)_2X$ (X = Br and AsF_6) [71,72], because $^{13}a_{\parallel}$ of TTF-CA is unknown. The hyperfine coupling tensor is mainly determined by the charge density of the HOMO of TTF, which is concentrated on the central carbons and sulfurs (Figure 9a) [73]. Thus, the difference in the molecular terminal structure between TTF (with hydrogens) and TMTTF (with methyl groups) is not influential on the HOMO density at the central carbon, namely, $^{13}a_{\parallel}$.

Then, according to the theoretical calculations of χ by Bonner and Fisher [74] and Estes et al. [75] for the uniform 1D AFHM, the experimental value of $\chi = 2.6 \times 10^{-5}$ emu/TTF mol projects an exchange interaction J of 5900 K, which is unrealistically large. On the other hand, in the scaling theory for the uniform 1D AFHM, the nuclear spin–lattice relaxation rate is expressed as $T_1^{-1} = a_\perp^2 D/\hbar J$, where $a_\perp$ is the hyperfine coupling component perpendicular to H, $\hbar$ is the reduced Planck constant, and D is a nonuniversal constant giving the magnitude of the dynamical spin susceptibility [76,77]. Using the values of J = 5900 K, D = 0.15 determined for the ideal 1D Heisenberg spin system Sr_2CuO_3 [77], and $^{13}a_\perp = 5.6$ kOe/μ_B for $(TMTTF)_2X$ (X = Br and AsF_6), $^{13}T_1^{-1}$ for 1D AFHM is calculated to be 1.1 s^{-1}, which is one order of magnitude smaller than the experimental value of $^{13}T_1^{-1} = 11$ s^{-1} at 14 kbar (Figure 9e). If J is evaluated from this formula, the resultant value of J = 580 K projects a χ value one order of magnitude larger than the experimental value. These estimations suggest that the spin state in the I_{para} phase cannot be described by the framework of the uniform 1D AFHM. This consequence, in conjunction with the observed dimer-liquid nature, strongly supports the picture that spins are not on each molecular site but dispersed on the boundaries between the fluctuating dimer domains.

Next, to demonstrate the emergence of mobile spin solitons, we measured the frequency dependence of $^1T_1^{-1}$, which gives the spectral density of local field fluctuations, $S(\omega)$, directly related to the soliton dynamics. We carried out measurements in the frequency range of 14–300 MHz at 300 K under 14 kbar in the I_{para} phase. $^1T_1^{-1}$ shows prominent frequency dependence, as shown in Figure 10; at high frequencies, $^1T_1^{-1}$ obeys the $\omega^{-1/2}$ law expected in the 1D diffusion, whereas it saturates to a constant value upon lowering the frequency. This behavior is well fitted by $T_1^{-1} = k_B T(\chi/N_A\mu_B^2)\gamma_N^2 a_{iso}^2 S_{1D\text{-}3D}(\omega_e)$ + const. [78,79], where a_{iso} is the isotropic part of the hyperfine coupling tensor, ω_e is the electron Larmor angular frequency, k_B is the Boltzmann constant, γ_N is the nuclear gyromagnetic ratio, and $S_{1D\text{-}3D}(\omega)$ is $S(\omega)$ in a 1D-3D crossover regime for the weakly coupled 1D systems described by [80]

$$S_{1D-3D}(\omega) = \frac{1}{\sqrt{2D_\parallel/\tau_\perp}}\left(\frac{1+\sqrt{1+(\omega\tau_\perp)^2}}{1+(\omega\tau_\perp)^2}\right)^{1/2}, \quad (1)$$

where $D_\parallel$ is the 1D diffusion rate, and $1/\tau_\perp$ is the 3D cutoff frequency. Fitting this formula to the experimental data gives $D_\parallel = 5.1 \times 10^{11}$ s^{-1} and $1/\tau_\perp = 5.6 \times 10^{10}$ s^{-1} with the use of $^1a_{iso}$ = −0.39 kOe/μ_B of TTF-BDT(Cu) [81]. Note that we neglect the anisotropic part of the hyperfine coupling tensor for simplicity. This result indicates that the spin solitons move diffusively along 1D chains with much slower interchain diffusion. The $D_\parallel$ value of the order of 10^{11} s^{-1} resides in between the frequency windows of the NQR (10^7 Hz) and infrared (10^{12} Hz) probes, which explains the seeming discrepancy between the NQR and infrared observations and is consistent with the temporally fluctuating dimer-liquid picture.

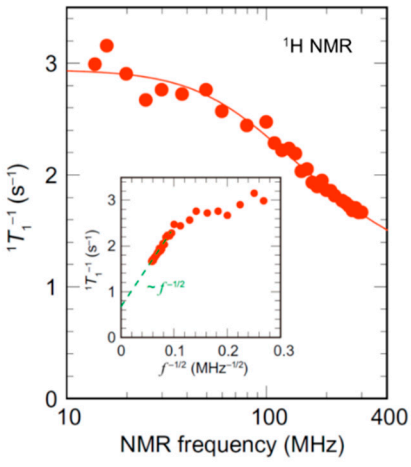

Figure 10. Frequency dependence of ^{1}H-NMR spin–lattice relaxation rate $^1T_1^{-1}$ at 300 K in the ionic paraelectric phase at 14 kbar. Red line is a fit to the data (see text and [17] for details). The inset is a plot of $^1T_1^{-1}$ against $f^{-1/2}$. Reprinted with permission from [17]. Copyright 2018, The Authors, some rights reserved; exclusive licensee AAAS. Distributed under a CC BY-NC 4.0 License (http://creativecommons.org/licenses/by-nc/4.0/(accessed on 30 November 2021)).

Here, the spin-soliton density, n_{ss}, is evaluated from the NMR results. Assuming that the spin solitons behave as Curie spins, $\chi = 2.6 \times 10^{-5}$ emu/TTF mol leads to 1 spin soliton per 25 donor–acceptor (DA) pairs at 285 K under 14 kbar. As another estimation of n_{ss}, if the cutoff time $\tau_\perp$ is determined by the collision between the soliton and antisoliton within the 1D chain, we can evaluate the average distance of solitons through the formula of the mean square displacement for the 1D diffusion described by $\langle x(t)^2 \rangle = 2D_\parallel t$. Substituting $D_\parallel = 5.1 \times 10^{11}$ s^{-1} and $t = \tau_\perp$ in this formula, the average distance of spin solitons is estimated to be ~10 DA pairs, which is comparable to $1/n_{ss} = 25$ DA pairs estimated from the absolute value of χ. Note that the origin of the 3D cutoff has been debatable; there are other conceivable mechanisms, such as the exchange interaction between the spin solitons on adjacent 1D chains or the hopping of solitons to neighbor chains. Thus, the obtained value of $1/n_{ss}$ ~ 10 DA pairs is a lower limit. Anyway, the spin soliton density in the I_{para} phase, 1 spin soliton per 10-25 DA pairs (n_{ss} ~ 0.02–0.05 spins per molecule), is much larger than $n_{ss} \sim 10^{-4}$ spins for frozen solitons in the I_{ferro} phase at ambient pressure [11], signifying that paramagnetic spin solitons are thermally excited only in the I_{para} phase.

During the long history of research on the NI transition since 1981, we successfully provided the first experimental evidence for thermally activated mobile spin solitons. As described in Section 2.2, the steady electrical current carried by the NIDW (or charge solitons) necessitates spin solitons. Thus, the existence of the mobile spin solitons verified by NMR also lends support to anomalous topological charge transport, described below.

4.2. Electrical Conductivity in the Neutral–Ionic Crossover Region: Neutral–Ionic Domain Wall

NMR studies demonstrated the mobile solitonic spin excitations emerging from the ferroelectric order. In the vicinity of the NI transition, another type of topological excitations, namely, NIDWs, can be activated [7–10,52]. The traveling of the two types of topological excitations is expected to lead to unconventional electrical transport. In this section, we review experimental demonstrations of anomalous electrical conduction by NIDWs and spin solitons [18]. Regarding electrical conductivity measurements, some experiments were previously conducted on TTF-CA. Our conductivity measurements differ from the previous ones in the following respects:

(i). We employed the four-terminal method to accurately evaluate the absolute value of the conductivity and the activation energy of charge transport (the two-terminal method was adopted in earlier studies [12,14]).
(ii). The anisotropy of the charge transport was evaluated by measuring the conductivity along the three crystal axes to reveal the nature of unconventional charge carriers.
(iii). We measured the electrical conductivity under finely tuned pressures with a Manganin wire used as a pressure gauge to monitor accurate pressure values near the NI crossover, which allowed us to estimate the activation energy from the conductivity profile along the inclined line parallel to the NI crossover line in the *P*-*T* plane, not at a fixed pressure.

Figure 11a,b show the temperature dependence of the electrical resistivity along the 1D chain (parallel to the *a*-axis) measured with the four-terminal method at fixed pressures. At lower pressures, the resistivity shows an anomaly at T_c and increases exponentially upon cooling, which is compatible with the previously reported two-terminal measurements [12,14]. With increasing pressure up to 9 kbar, the absolute value of resistivity at ambient temperature decreases, and the kink structure at T_c becomes rounded. In the pressure range between 6.6 and 7.5 kbar, the resistivity apparently shows metallic behavior above T_c. At pressures higher than 9 kbar, the resistivity monotonically increases with

a slight kink around T_c. Figure 11c shows the contour plot of the *a*-axis conductivity, σ_a, which illustrates a highly conducting state just in the NI crossover region; σ_a reaches a maximum value of 7 S/cm at ~9 kbar (Figure 12a). This value is comparable to the conductivities of organic conductors at room temperature.

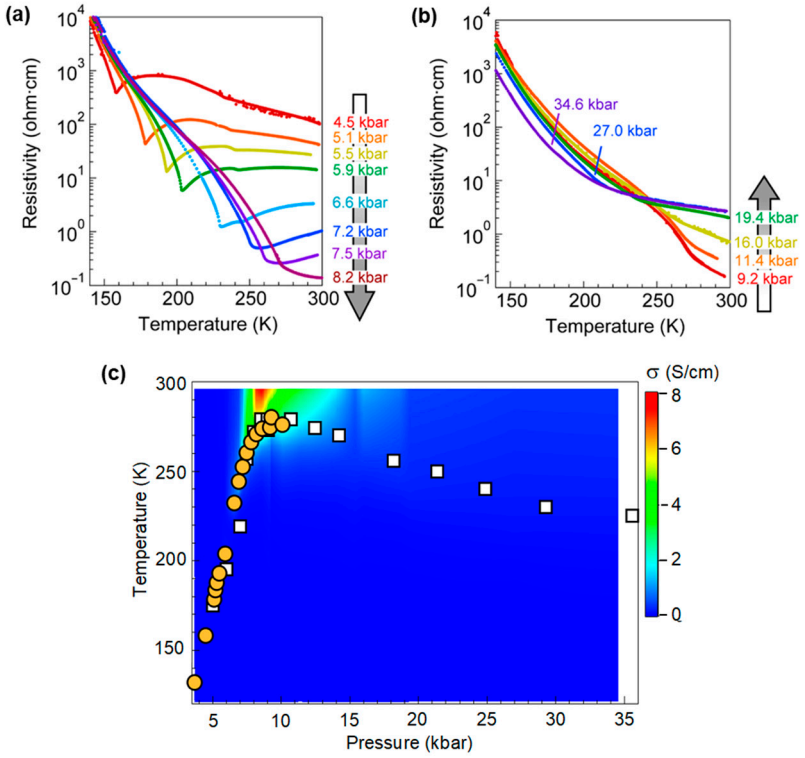

Figure 11. (**a**,**b**) Temperature profiles of the electrical resistivity along the *a*-axis (1D direction) at fixed pressures. (**c**) Contour plot of the electrical conductivity along the *a*-axis σ_a on the pressure–temperature phase diagram. Orange circles represent the phase transition temperatures T_c determined by the kink temperatures of σ_a. Open squares represent T_c determined by NQR measurements [16]. Reprinted with permission from [18]. Copyright 2019, The Authors, some rights reserved; exclusive licensee AAAS. Distributed under a CC BY-NC 4.0 License (http://creativecommons.org/licenses/by-nc/4.0/(accessed on 15 November 2021)).

The anisotropies of conductivity, σ_a/σ_b and σ_a/σ_c, are also enhanced in association with the peak of σ_a at the same pressure of ~9 kbar (see Figure 12a,b), indicating that the charge carriers resulting in high conductivity in the NI crossover are strongly confined in the 1D chains. Remarkably, this enhancement of conductivity appears between the two insulating phases: the band insulator for the N phase and the ionic Mott insulator for the I phase. These features suggest that the highly conductive charge carriers are associated with unconventional excitations, such as topological NIDW excitations, as previously predicted [12,14,48]. Unbound NIDWs have no way to hop into adjacent chains, resulting in highly 1D transport confined in the chain. Optical measurements indicate that the N and I states dynamically coexist near 9 kbar [34], which accords with the picture that the mobile NIDWs separating the N and I domains are excited in this region. The previously found NIDWs at ambient pressure were in the vicinity of the N-to-I_{ferro} phase transition, and thus, NIDW motion was restricted due to the long-range dimer order. In contrast to this, NIDWs activated near the crossover between the N and I_{para} phase without the dimer order can travel freely to carry the charge current.

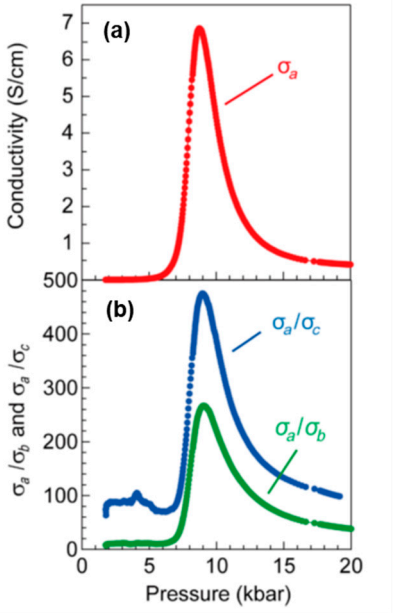

Figure 12. Pressure profiles of electrical conductivity along the *a*-axis σ_a (**a**) and the anisotropies of conductivity, σ_a/σ_b and σ_a/σ_c (**b**), at ambient temperature. Reprinted with permission from [18]. Copyright 2019, The Authors, some rights reserved; exclusive licensee AAAS. Distributed under a CC BY-NC 4.0 License (http://creativecommons.org/licenses/by-nc/4.0/(accessed on 15 November 2021)).

To evaluate the activation energy of the NIDW, we performed more detailed resistivity measurements under finely tuned pressures near the NI crossover region. As mentioned above, the temperature profile of resistivity at fixed pressures appears to be of metallic nature near the NI crossover (Figure 11a). This is probably because the NI crossover line denoted by $P_c(T)$, which is determined as the pressure at which the conductivity shows a peak at a fixed temperature, is tilted in the *P*-*T* plane (see Figure 13a), and the activation energy of the NIDW depends on the deviation from the NI crossover line, $\Delta P = P - P_c$. Indeed, the conductivity along inclined lines parallel to the NI crossover line (at $\Delta P = 0$) shows insulating behavior, as shown in Figure 13b. Its Arrhenius plot gives the activation energy E_g of 0.055 eV, which is one order of magnitude smaller than half of the charge-transfer excitation energy, 0.6–0.7 eV [21,82]; it is rather comparable to the theoretically predicted NIDW excitation energy of 0.07–0.08 eV [48]. Moreover, as shown in Figure 13c, the ΔP dependence of E_g reaches a minimum at $\Delta P = 0$, which is also consistent with quantum Monte Carlo simulations [48]. These features suggest that the thermally excited NIDWs dividing the two topologically different domains are responsible for the anomalously high and 1D-confined electrical conductivity.

Here, we estimate the NIDW density, n_{DW}, by mapping the NI transition system to a 1D Ising model [83], which is valid for TTF-CA situated at the NI boundary where the N and I states are degenerate. In this case, the NIDW corresponds to a spinon in the Ising spin system (the N and I states correspond to the up and down spins, respectively). Thus, the correlation length in the Ising model, $\xi \sim 1/\ln(\coth(E_{DW}/2k_BT))$, roughly gives the average distance between the NIDWs; n_{DW} is given by $n_{DW} \sim 1/2\xi \sim \ln(\coth(E_{DW}/2k_BT))/2$. Using $E_{DW} = 0.055$ eV evaluated at $\Delta P = 0$, n_{DW} is estimated at 1 NIDW per ~5 DA pairs on the NI crossover line at ambient temperature. This value is compared to the spin soliton density n_{ss}, 1 spin soliton per 10–25 DA pairs, as described in Section 4.1. Considering that ~10 DA pairs contain one I domain on average, it turns out that a considerable fraction of the I domains contain a spin soliton. This situation is in agreement with the theoretically suggested picture that NIDWs carry the stationary electrical current in cooperation with spin solitons [7,9,10].

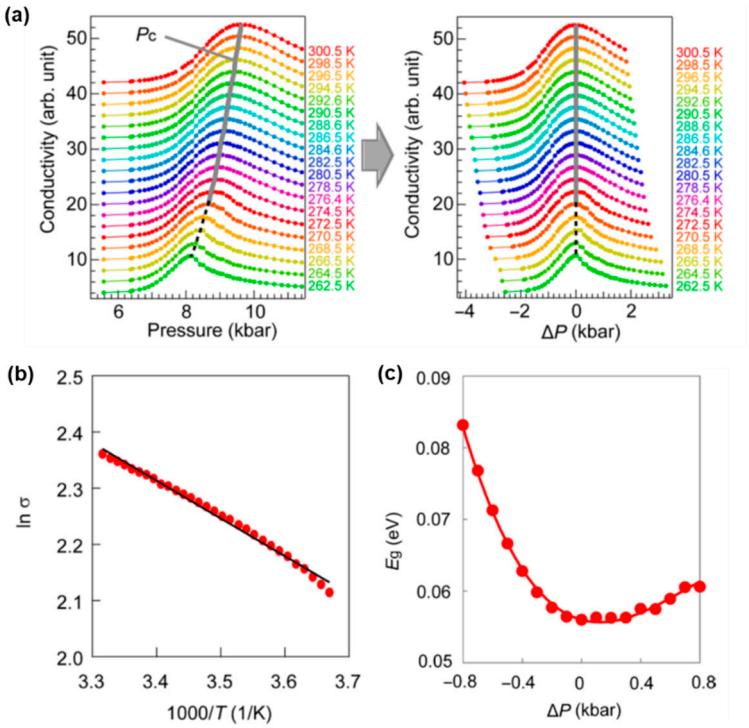

Figure 13. (**a**) Electrical conductivity under finely tuned pressures at fixed temperatures (left panel). Plot of conductivity against $\Delta P = P - P_c$ (right panel). P_c is determined by the peak pressure of conductivity at a given temperature. (**b**) Activation plot of conductivity at $\Delta P = 0$. Black line is a fit of the single-exponential function to conductivity. (c) Activation energy, E_g, evaluated at various ΔP. Reprinted with permission from [18]. Copyright 2019, The Authors, some rights reserved; exclusive licensee AAAS. Distributed under a CC BY-NC 4.0 License (http://creativecommons.org/licenses/by-nc/4.0/(accessed on 15 November 2021)).

Why are spin solitons required for a steady electrical current? We briefly explain the transport mechanism by topological excitations using the schematic illustrations depicted in Figure 14, where the N and I states are represented as D^0A^0 and D^+A^-, respectively, for simplicity.

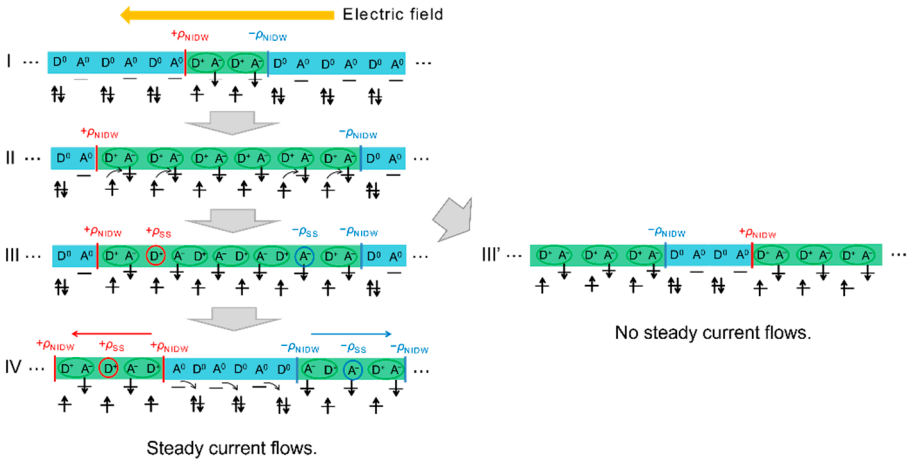

Figure 14. Schematic illustrations of the mechanism of the steady electrical current carried by topological excitations. The neutral and ionic states are represented as D^0A^0 and D^+A^-, respectively, for simplicity. Reprinted with permission from [18]. Copyright 2019, The Authors, some rights reserved; exclusive licensee AAAS. Distributed under a CC BY-NC 4.0 License (http://creativecommons.org/licenses/by-nc/4.0/(accessed on 15 November 2021)).

Step I: A pair of NIDWs with effective charges, $+\varrho_{NIDW}$ and $-\varrho_{NIDW}$, is thermally excited in an N domain, where $\pm\varrho_{NIDW}$ is the topological charge of $\pm e(\varrho_I - \varrho_N)/2$.

Step II: An electric field applied to the left separates NIDWs with $+\rho_{NIDW}$ and $-\rho_{NIDW}$ in opposite directions to expand the I_B domain with the D^+A^- pattern.

Step III: A pair of spin solitons with effective charges, $+\varrho_{SS}$ and $-\varrho_{SS}$, is thermally excited in the I_B domain, where $\pm\rho_{SS}$ is the topological charge of $\pm e(1 - \varrho_I)$. It generates an I_A domain with the oppositely polarized A^-D^+ pattern to the I_B domain, which has the D^+A^- pattern.

Step IV: A pair of NIDWs is excited in the I_A domain and grows to an N domain due to an electron transfer to the right.

Consequently, the positive charges, $+\varrho_{NIDW}$ and $+\varrho_{SS}$, and the negative charges, $-\varrho_{NIDW}$ and $-\varrho_{SS}$, flow to the left and right, respectively, giving a steady electrical current. If the spin solitons are absent, Step III is replaced with Step III': allowed excitations of the NIDW pair in the I_B domain are those with $-\varrho_{NIDW}$ and $+\varrho_{NIDW}$ on the left and right sides, respectively, which are not separated from each other but are recombined under this electric field configuration, resulting in no steady current. In short, the steady current necessitates excitations of oppositely polarized I domains, which are made possible by spin soliton excitations. Thus, the presence of spin solitons is crucial for the generation of steady current, as theoretically proposed [7,9,10].

Finally, we discuss the electrical conduction carried by topological excitations in the N and I_{para} phases far from the NI crossover. In Figure 15, the pressure dependence of conductivity is shown along with that of ^{13}C-NMR $^{13}T_1^{-1}$ to compare the behaviors of spin and charge excitations. For $P < P_c$, $^{13}T_1^{-1}$ exhibits an exponential decrease as the system departs from the NI crossover, which is scaled to the conductivity. On the other hand, when the system enters the I_{para} phase for $P > P_c$, the conductivity begins to decline, whereas $^{13}T_1^{-1}$ retains large values. These suggest that the charge and spin degrees of freedom are coupled in the N phase, whereas they are decoupled in the I phase. The behavior of the N phase is explainable if the charge carrier is a polaron or equivalently coupled charge and spin solitons with an unfractionalized charge of $\pm e$ and a spin of 1/2, which carries charge and spin inseparably, as depicted in Figure 16. In the I phase away from the NI crossover, the N domain shrinks to form a charge soliton sandwiched by two NIDWs, whose density decreases with pressure. This explains why conductivity decreased when P increased from P_c. Conversely, the spin solitons responsible for the $^{13}T_1^{-1}$ behavior are likely to be more excited because their excitation energy is diminished for P higher than P_c, as theoretically suggested [7,9,10]. These decoupled behaviors of charge and spin solitons explain the observation shown in Figure 15. We note that the steady current in the I phase needs both charge and spin solitons, and the conductivity is governed by the density of minor carriers, which are charge solitons. The quantitative estimation of the charge soliton density in the I_{para} phase is described in Section 4.3.

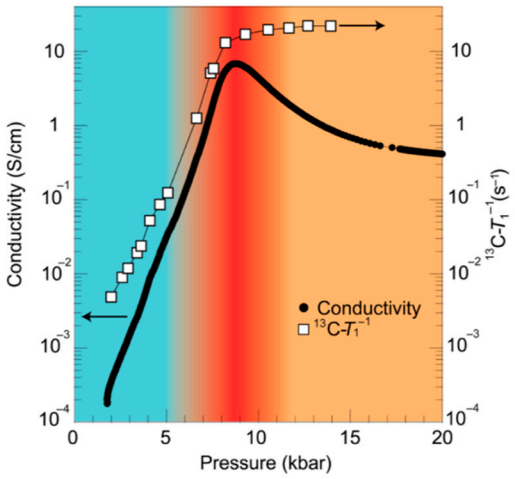

Figure 15. Pressure profiles of the electrical conductivity (closed circles) and ^{13}C-NMR spin–lattice relaxation rate $^{13}T_1^{-1}$ (open squares) at ambient temperature. The blue-, red-, and orange-colored regions roughly indicate the neutral phase, NI crossover region, and ionic phase, respectively. Reprinted with permission from [18]. Copyright 2019, The Authors, some rights reserved; exclusive licensee AAAS. Distributed under a CC BY-NC 4.0 License (http://creativecommons.org/licenses/by-nc/4.0/(accessed on 15 November 2021)).

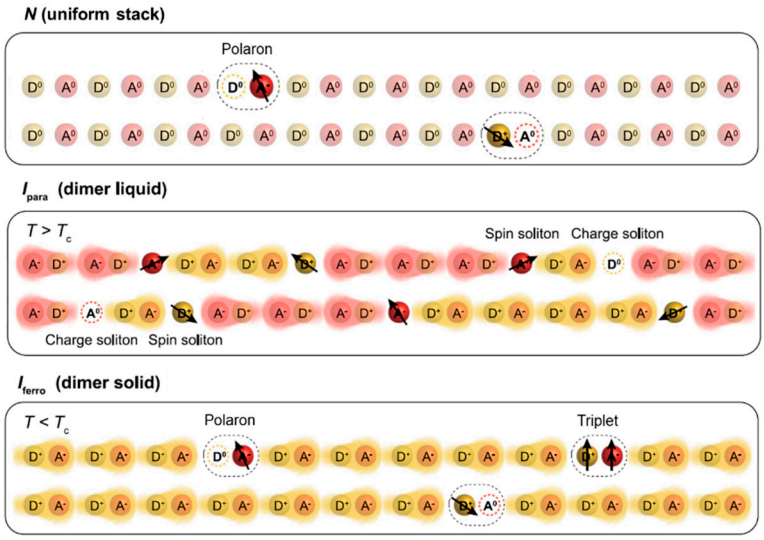

Figure 16. Schematic illustrations of the spin and charge excitations in the neutral (N), ionic paraelectric (I_{para}), and ferroelectric (I_{ferro}) phases. The neutral and ionic states are represented as D^0A^0 and D^+A^- with degrees of charge transfer $\varrho = 0$ and 1, respectively, for simplicity, although ϱ takes intermediate values in the neutral and ionic states in reality. The lower two panels are reprinted with permission from [19]. Copyright 2021, American Physical Society.

4.3. Binding Transition of Solitons upon Space-Inversion Symmetry-Breaking Ferroelectric Order

The mobile topological excitations mentioned in Sections 4.1 and 4.2 emerge only in the nonordered paraelectric regime; these are not vital in the long-range ordered phase because free solitons, if any, would interrupt the long-ranged order [84]. What form do the spin and charge excitations take in the long-range ordered phase? How do solitons detected in the nonordered paraelectric regime conform to the 3D ferroelectric ordered state? In this section, we review the studies on the profiles of spin and charge excitations upon entering the long-range ferroelectric ordered (I_{ferro}) phase from the nonordered I_{para} phase by resistivity, NMR, and NQR measurements [19], the goal of which is to pursue the fate of spin-soliton–charge-soliton composite matter upon the space-inversion symmetry-breaking ferroelectric order.

Before we present the experimental results, to make it clear that the dimer-liquid I_{para} phase of TTF-CA is soliton matter, we evaluated the charge soliton density n_{cs} in the I_{para} phase at 14 kbar using the resistivity data shown in Section 4.2. The electrical transport study strongly suggested that the charge solitons reside in the I_{para} phase because the resistivity in the I_{para} phase is much smaller than that in the N phase (see Figure 15) [18,85]. At 9 kbar in the NI crossover region, the NIDW density, n_{DW}, was estimated at about 1 per 5 DA pairs. As described in Section 4.2, the bound NIDWs sandwiching an N molecule form the charge soliton in the I phase, so $n_{cs} = n_{DW}/2$. At ambient temperature, the σ value at 9 kbar is reduced by an order of magnitude at 14 kbar (see Figure 15), which suggests that n_{cs} is 1 per ~100 DA pairs at 14 kbar, assuming that the pressure dependence of σ depends on only the charge carrier density. On the other hand, the spin-soliton density, n_{ss}, is 1 per 10–25 DA pairs, as deduced from NMR data (see Section 4.1). Thus, the I_{para}

phase at 14 kbar hosts soliton matter composed of spin solitons (majority) and charge solitons (minority) with a 10:1–4:1 population (see Figure 16).

First, we performed ^{13}C-NMR measurements at 14 kbar to examine the nature of spin excitations. As shown in Figure 17a,b, both the spin shift, S, and $^{13}T_1^{-1}$ exhibit clear kinks at T_c ~ 270 K, below which they decrease upon cooling, consistent with the nonmagnetic state of the I_{ferro} phase. However, the slopes in their Arrhenius plots are different (see Figure 17c); the spin shift multiplied by temperature follows $TS \propto \exp(-\Delta_s/k_BT)$ with a spin excitation gap Δ_s of 3240 K for 200 K < T < T_c, whereas the variation in $^{13}T_1^{-1}$ is more gradual in the same temperature range, although the activation energy is not well defined. Here, we discuss the large gap of Δ_s = 3240 K. For conventional spin-Peierls systems, T_c and the singlet–triplet gap Δ hold the relation Δ/k_BT_c ~ 1.76 (the BCS relationship) or 2.47 (obtained with a bosonization method [86]). In the present case, however, Δ_s/k_BT_c yields ~12, which is too large to regard the I_{para}-to-I_{ferro} phase transition as the conventional spin-Peierls transition for 1D Heisenberg spins, supporting the picture that the I_{para} phase hosts mobile spin solitons (see Sections 4.1 and 4.2).

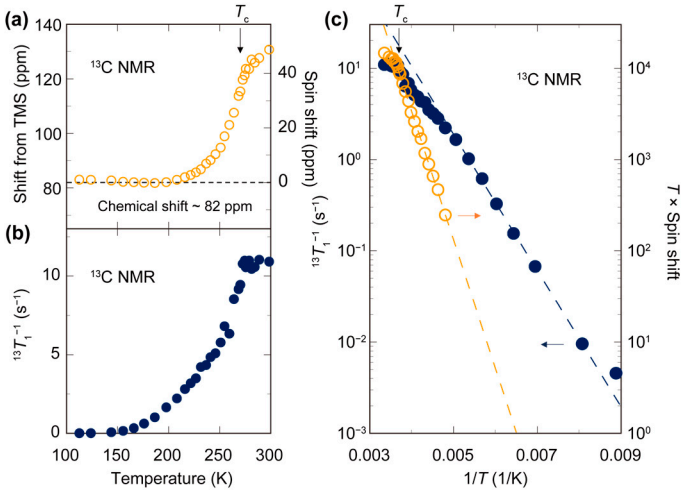

Figure 17. Temperature dependence of ^{13}C-NMR spectral shift (**a**) and spin–lattice relaxation rate $^{13}T_1^{-1}$ (**b**) at 14 kbar. (**c**) Activation plots of spin shift multiplied by temperature (orange open circles) and $^{13}T_1^{-1}$ (blue closed circles). Reprinted with permission from [19]. Copyright 2021, American Physical Society.

Next, we discuss the difference between the decreases in the spin shift and $^{13}T_1^{-1}$ below T_c. For conventional singlet–triplet excitations, the temperature profiles of S and T_1^{-1} in the spin-singlet phase should not significantly differ [87]. Thus, the observed behaviors of S and T_1^{-1} imply the presence of at least two types of spin excitations below T_c. In the I_{ferro} phase, soliton excitations should be in pairs so as not to violate the 3D ferroelectric order (see Figure 16); one is the triplet spin soliton pair excitation of charge-neutral spin 1, and the other is the spin soliton–charge soliton pair excitation, equivalently polarons, with a charge e and a spin 1/2, as discussed for conducting polymers [3]. The polarons carry not only spins but also charges without violating the ferroelectric dimer order in the I_{ferro} phase. As estimated above, the spin soliton density n_{ss} is larger than the charge soliton density n_{cs} in the I_{para} phase above T_c, suggesting that the magnetism just below T_c should be dominated by bound spin soliton pairs, whose triplet excitations cause a steep decrease in the spin shift. On the other hand, well below T_c, where triplet excitations with a large gap of 3240 K almost vanish, the polaron contribution is expected to be dominant in $^{13}T_1^{-1}$. These pictures signify that the I_{para}-to-I_{ferro} phase transition is a binding transition of solitons upon the symmetry-breaking dimer order.

To seek further evidence for the emergence of polarons, we investigated the lattice properties using ^{35}Cl-NQR spectroscopy. The motion of polarons should be followed by

lattice distortion. Thus, the ^{35}Cl-NQR spin–lattice relaxation rate $^{35}T_1^{-1}$, probing the lattice fluctuations through nuclear quadrupolar interaction, gives valuable insights into the lattice dynamics. $^{35}T_1^{-1}$ exhibits a divergent peak at T_c, which is attributable to the critical lattice fluctuations associated with the 3D ferroelectric dimerization transition, and becomes suppressed upon cooling (see Figure 18). Below 140 K, $^{35}T_1^{-1}$ roughly obeys the T^2 law, which is the conventional phonon contribution by the two-phonon Raman process [88]. Above 140 K, however, $^{35}T_1^{-1}$ is drastically enhanced from the T^2 law, indicating that another relaxation mechanism appears. Remarkably, it is scaled to $^{13}T_1^{-1}$ for $140 < T < 250$ K ($< T_c$), signifying that the quadrupolar and magnetic relaxations are attributed to common excitations. This strongly indicates that the spin carriers causing the magnetic relaxation below 250 K are not conventional band quasiparticles but polarons dragging lattice distortion.

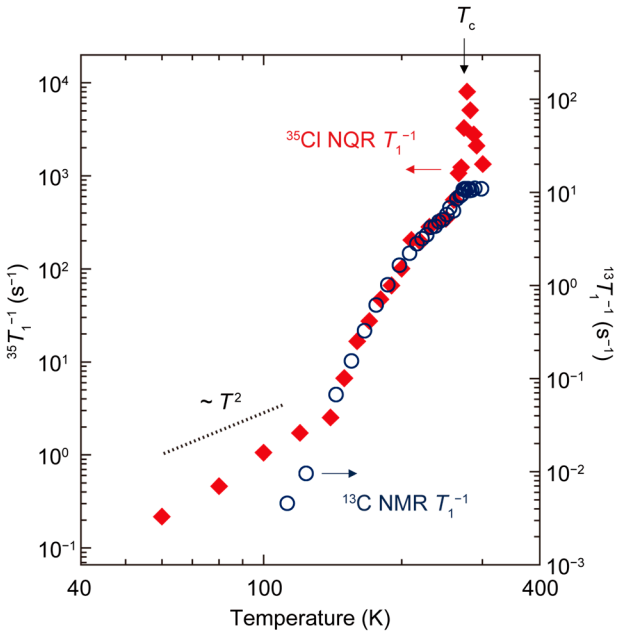

Figure 18. Comparison between the ^{35}Cl-NQR and ^{13}C-NMR spin–lattice relaxation rates, $^{35}T_1^{-1}$ (red closed diamonds) and $^{13}T_1^{-1}$ (blue open circles), at 14 kbar. Reprinted with permission from [19]. Copyright 2021, American Physical Society.

Polarons also carry an electrical current. Figure 19a shows the temperature dependence of electrical resistivity at 14 kbar, which exhibits insulating behavior below ambient temperature with a slight kink at T_c. The activation energy of conductivity σ is evaluated to be $\Delta_\sigma \sim 2100$ K in the I_{ferro} phase (see the inset of Figure 19a). If the band quasiparticles are carriers, Δ_σ would be larger than half of the charge-transfer gap of ~0.7 eV (~8100 K) evaluated in optical studies [21,82]. Thus, the substantially lower charge excitation gap suggests that polarons with excitation energies reduced by lattice relaxation are carriers of electrical current in the I_{ferro} phase, distinct from the band quasiparticle excitations.

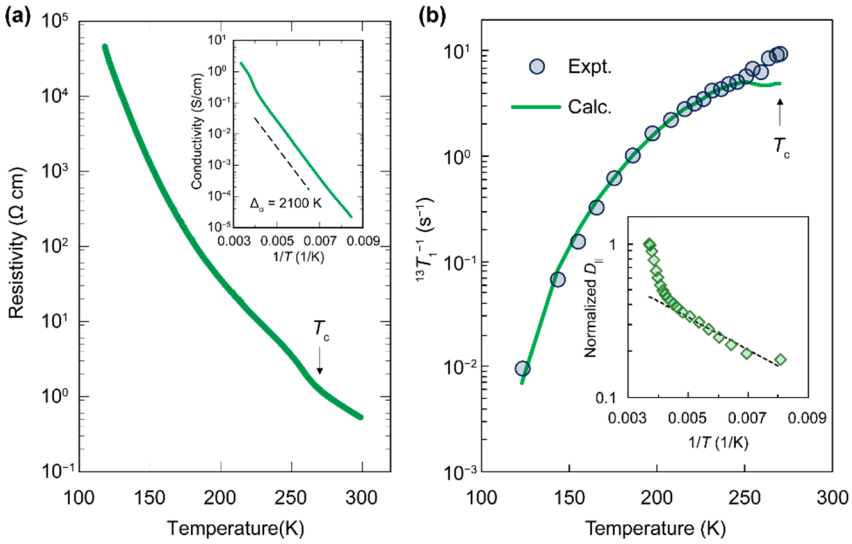

Figure 19. (**a**) Temperature dependence of electrical resistivity at 14 kbar. Inset: Activation plot of electrical conductivity at 14 kbar. (**b**) Comparison between the experimental $^{13}T_1^{-1}$ and the calculated polaron contribution to $^{13}T_1^{-1}$, $(^{13}T_1^{-1})_P$ (see text). The inset shows the normalized 1D diffusion constant. Reprinted with permission from [19]. Copyright 2021, American Physical Society.

We demonstrated that there are two types of spin excitations in the I_{ferro} phase: the triplet-type bound spin soliton pairs and the polaronic bound pairs of spin and charge solitons (Figure 16). Finally, we tried to distinguish the two contributions to magnetism. When the polarons move diffusively, the polaron contribution to $^{13}T_1^{-1}$, $(^{13}T_1^{-1})_P$, is expressed as $(^{13}T_1^{-1})_P \propto n_P/\sqrt{aD_\parallel}$, where n_P is the density of the polarons, a is the anisotropy parameter defined by $D_\perp/D_\parallel$, and $D_\parallel$ ($D_\perp$) is the diffusion constant of the polarons parallel (perpendicular) to the 1D chain. On the other hand, σ is expressed as $\sigma = n_P e^2 D_\parallel/k_B T$. By combining the two equations and assuming that n_P obeys the activation form (see [19] for details), the temperature profile of $D_\parallel$ is obtained, as shown in the inset of Figure 19b. Note that we used the anisotropy of conductivity as a [19]. At low temperatures, $D_\parallel$ shows an activation behavior with an energy barrier of 240 K, which is remarkably near the Peierls-coupled optical phonon frequencies of ~120–180 K in the I_{ferro} phase [89]. This suggests that the polarons thermally hop over the energy barrier with the assistance of Peierls phonons. By substituting the obtained $D_\parallel$ value and the activation form of n_P in the above formula of $(^{13}T_1^{-1})_P$, we evaluate $(^{13}T_1^{-1})_P$ as shown in Figure 19b, which nearly coincides with the experimental $^{13}T_1^{-1}$ below 250 K; however, at 250 K < T < T_c, the experimental values deviate upward from $(^{13}T_1^{-1})_P$. This additional contribution is very probably the triplet excitations of bound spin soliton pairs with a large gap of Δ_s = 3240 K that appear only just below T_c because the majority are spin solitons in the I_{para} phase above T_c.

The binding transition of solitons has never been observed in a conducting polymer, which does not show a 3D order. Thus, the presented finding of the soliton organization upon the symmetry-breaking transition revealed novel aspects of soliton physics that have ever been studied in one dimension.

5. Summary

In this review, we report recent progress in the study of mobile topological spin and charge excitations in a neutral–ionic (NI) transition system, TTF-CA. The solitons and neutral–ionic domain walls (NIDWs) reported in the past were frozen defects and could not carry an electrical current because these excitations were locked due to the long-range dimer order. In contrast to these observations, we captured mobile topological excitations that are thermally excited in the nonordered paraelectric phase in TTF-CA, as summarized below:

(i). The revisited pressure–temperature phase diagram contains the paraelectric ionic (I_{para}) phase extended in the high-pressure region up to 35 kbar. The N-to-I_{para} phase boundary is a crossover, not a phase transition. The I_{para} phase hosts the dimer-liquid state, providing a chance for the emergence of mobile NIDWs near the N-to-I_{para} crossover and solitons in the I_{para} phase.

(ii). In the I_{para} phase, spin solitons are thermally excited as mobile boundaries dividing fluctuating dimer domains in 1D chains and contribute to the anomalous topological charge transport in cooperation with the NIDW.

(iii). Near the N-to-I_{para} crossover, mobile NIDWs with topological charges carry 1D-confined large electrical conduction in cooperation with spin solitons. This is the first demonstration of the topological charge transport carried by NIDWs and spin solitons in the NI transition system.

(iv). In the 3D ferroelectric ordered (I_{ferro}) phase, spin solitons and charge solitons that are free in the I_{para} phase undergo a binding transition to form two-component composite pairings: neutral spin soliton pairs and polaronic spin-soliton–charge-soliton pairs. The polaronic pairs carry magnetism and electrical conduction with the assistance of Peierls-coupled optical phonons.

The topological charge transport revealed here is not the one that occurs in topological boundaries, as has been extensively studied in topological insulators, but originates from the excitations and motions of the topological boundaries themselves. This novel charge transport is a significant addition to soliton physics, which has been developed mainly for conducting polymers, and is expected to open a novel paradigm for broad transport-related phenomena such as thermoelectric effects.

Author Contributions: K.S. wrote the manuscript with the assistance of K.K. R.T., K.M. and H.O. commented on the manuscript. All authors have read and agreed to the published version of the manuscript.

Funding: This work was supported by the JSPS Grant-in-Aids for Scientific Research (Grant Numbers JP25220709, JP16H06346, JP17K05532, JP17K05846, JP18H05225, JP19H01846, JP20K20894, JP20KK0060, JP21K18144, and JP21H04988); by the Japan Science and Technology Agency, CREST (Grant Number JPMJCR1661); by the Mitsubishi Foundation (Grant Number 202110014); and by the Murata Science Foundation.

Institutional Review Board Statement: Not applicable.

Informed Consent Statement: Not applicable.

Data Availability Statement: Not applicable.

Acknowledgments: We would like to thank F. Iwase, M. Hosoda, T. Nishikawa, A. Katougi, S. Horiuchi, R. Kato, and T. Miyamoto for their experimental collaborations. We also thank H. Fukuyama, N. Nagaosa, and M. Ogata for fruitful discussions.

Conflicts of Interest: The authors declare no conflict of interest.

References

1. Kosterlitz, J.M.; Thouless, D.J. Ordering, metastability and phase transitions in two-dimensional systems. *J. Phys. C Solid State Phys.* **1973**, *6*, 1181–1203. https://doi.org/10.1088/0022-3719/6/7/010.
2. Thouless, D.J.; Kohmoto, M.; Nightingale, M.P.; Nijs, M. den Quantized Hall conductance in a two dimensional periodic potential. *Phys. Rev. Lett.* **1982**, *49*, 405–408.
3. Heeger, A.J.; Kivelson, S.; Schrieffer, J.R.; Su, W.P. Solitons in conducting polymers. *Rev. Mod. Phys.* **1988**, *60*, 781–850. https://doi.org/10.1103/RevModPhys.60.781.
4. Wen, X.G. Topological orders and edge excitations in fractional quantum Hall states. *Adv. Phys.* **1995**, *44*, 405–473. https://doi.org/10.1080/00018739500101566.
5. Brazovskii, S. Ferroelectricity and Charge Ordering in Quasi One-Dimensional Organic Conductors. In *The Physics of Organic Superconductors and Conductors*; Lebed, A., Ed.; Springer: Berlin/Heidelberg, Germany, 2008; pp. 313–355.
6. Hasan, M.Z.; Kane, C.L. Colloquium: Topological insulators. *Rev. Mod. Phys.* **2010**, *82*, 3045–3067. https://doi.org/10.1103/RevModPhys.82.3045.

7. Nagaosa, N. Theory of neutral-ionic transition in organic crystals. III. Effect of the electron-lattice interaction. *J. Phys. Soc. Jpn.* **1986**, *55*, 2754–2764. https://doi.org/10.1143/JPSJ.55.2754.
8. Soos, Z.G.; Painelli, A. Metastable domains and potential energy surfaces in organic charge-transfer salts with neutral-ionic phase transitions. *Phys. Rev. B* **2007**, *75*, 155119. https://doi.org/10.1103/PhysRevB.75.155119.
9. Fukuyama, H.; Ogata, M. Solitons in the crossover between band insulator and Mott insulator: Application to TTF-Chloranil under pressure. *J. Phys. Soc. Jpn.* **2016**, *85*, 023702. https://doi.org/10.7566/JPSJ.85.023702.
10. Tsuchiizu, M.; Yoshioka, H.; Seo, H. Phase competition, solitons, and domain walls in neutral-ionic transition systems. *J. Phys. Soc. Jpn.* **2016**, *85*, 104705. https://doi.org/10.7566/JPSJ.85.104705.
11. Mitani, T.; Saito, G.; Tokura, Y.; Koda, T. Soliton formation at the neutral-to-ionic phase transition in the mixed-stack charge-transfer crystal tetrathiafulvalene-*p*-chloranil. *Phys. Rev. Lett.* **1984**, *53*, 842–845. https://doi.org/10.1103/PhysRevLett.53.842.
12. Mitani, T.; Kaneko, Y.; Tanuma, S.; Tokura, Y.; Koda, T.; Saito, G. Electric conductivity and phase diagram of a mixed-stack charge-transfer crystal: Tetrathiafulvalene-*p*-chloranil. *Phys. Rev. B* **1987**, *35*, 427–429. https://doi.org/10.1103/PhysRevB.35.427.
13. Tokura, Y.; Okamoto, H.; Koda, T.; Mitani, T.; Saito, G. Nonlinear electric transport and switching phenomenon in the mixed-stack charge-transfer crystal tetrathiafulvalene-*p*-chloranil. *Phys. Rev. B* **1988**, *38*, 2215–2218. https://doi.org/10.1103/PhysRevB.38.2215.
14. Okamoto, H.; Komatsu, T.; Iwasa, Y.; Koda, T.; Tokura, Y.; Koshihara, S.; Mitani, T.; Saito, G. Dynamical aspects of neutral-ionic phase transition in organic charge-transfer complex crystals. *Synth. Met.* **1988**, *27*, 189–196. https://doi.org/10.1016/0379-6779(88)90143-9.
15. Okamoto, H.; Mitani, T.; Tokura, Y.; Koshihara, S.; Komatsu, T.; Iwasa, Y.; Koda, T.; Saito, G. Anomalous dielectric response in tetrathiafulvalene-*p*-chloranil as observed in temperature- and pressure-induced neutral-to-ionic phase transition. *Phys. Rev. B* **1991**, *43*, 8224–8232. https://doi.org/10.1103/PhysRevB.43.8224.
16. Takehara, R.; Sunami, K.; Iwase, F.; Hosoda, M.; Miyagawa, K.; Miyamoto, T.; Okamoto, H.; Kanoda, K. Revisited phase diagram on charge instability and lattice symmetry breaking in the organic ferroelectric TTF-QCl_4. *Phys. Rev. B* **2018**, *98*, 054103. https://doi.org/10.1103/PhysRevB.98.054103.
17. Sunami, K.; Nishikawa, T.; Miyagawa, K.; Horiuchi, S.; Kato, R.; Miyamoto, T.; Okamoto, H.; Kanoda, K. Evidence for solitonic spin excitations from a charge-lattice-coupled ferroelectric order. *Sci. Adv.* **2018**, *4*, eaau7725. https://doi.org/10.1126/sciadv.aau7725.
18. Takehara, R.; Sunami, K.; Miyagawa, K.; Miyamoto, T.; Okamoto, H.; Horiuchi, S.; Kato, R.; Kanoda, K. Topological charge transport by mobile dielectric-ferroelectric domain walls. *Sci. Adv.* **2019**, *5*, eaax8720. https://doi.org/10.1126/sciadv.aax8720.
19. Sunami, K.; Takehara, R.; Katougi, A.; Miyagawa, K.; Horiuchi, S.; Kato, R.; Miyamoto, T.; Okamoto, H.; Kanoda, K. Fate of soliton matter upon symmetry-breaking ferroelectric order. *Phys. Rev. B* **2021**, *103*, 134112. https://doi.org/10.1103/PhysRevB.103.134112.
20. McConnell, H.M.; Hoffman, B.M.; Metzger, R.M. Charge transfer in molecular crystals. *Proc. Natl. Acad. Sci. USA* **1965**, *53*, 46–50.
21. Torrance, J.B.; Vazquez, J.E.; Mayerle, J.J.; Lee, V.Y. Discovery of a neutral-to-ionic phase transition in organic materials. *Phys. Rev. Lett.* **1981**, *46*, 253–257.
22. Buron-Le Cointe, M.; Collet, E.; Toudic, B.; Czarnecki, P.; Cailleau, H. Back to the structural and dynamical properties of neutral-ionic phase transitions. *Crystals* **2017**, *7*, 285. https://doi.org/10.3390/cryst7100285.
23. Torrance, J.B.; Girlando, A.; Mayerle, J.J.; Crowley, J.I.; Lee, V.Y.; Batail, P.; LaPlaca, S.J. Anomalous nature of neutral-to-ionic phase transition in tetrathiafulvalene-chloranil. *Phys. Rev. Lett.* **1981**, *47*, 1747–1750. https://doi.org/10.1103/PhysRevLett.47.1747.
24. Tokura, Y.; Koda, T.; Mitani, T.; Saito, G. Neutral-to-ionic transition in tetrathiafulvalene-*p*-chloranil as investigated by optical reflection spectra. *Solid State Commun.* **1982**, *43*, 757–760. https://doi.org/10.1016/0038-1098(82)90986-3.
25. Girlando, A.; Marzola, F.; Pecile, C.; Torrance, J.B. Vibrational spectroscopy of mixed stack organic semiconductors: Neutral and ionic phases of tetrathiafulvalene–chloranil (TTF–CA) charge transfer complex. *J. Chem. Phys.* **1983**, *79*, 1075–1085. https://doi.org/10.1063/1.445833.
26. Dressel, M.; Peterseim, T. Infrared investigations of the neutral-ionic phase transition in TTF-CA and its dynamics. *Crystals* **2017**, *7*, 17. https://doi.org/10.3390/cryst7010017.
27. Masino, M.; Castagnetti, N.; Girlando, A. Phenomenology of the neutral-ionic valence instability in mixed stack charge-transfer crystals. *Crystals* **2017**, *7*, 108. https://doi.org/10.3390/cryst7040108.
28. Kagawa, F.; Horiuchi, S.; Tokura, Y. Quantum phenomena emerging near a ferroelectric critical point in a donor–acceptor organic charge-transfer complex. *Crystals* **2017**, *7*, 106. https://doi.org/10.3390/cryst7040106.
29. Morimoto, T.; Miyamoto, T.; Okamoto, H. Ultrafast electron and molecular dynamics in photoinduced and electric-field-induced neutral–ionic transitions. *Crystals* **2017**, *7*, 132. https://doi.org/10.3390/cryst7050132.
30. D'Avino, G.; Painelli, A.; Soos, Z.G. Modeling the neutral-ionic transition with correlated electrons coupled to soft lattices and molecules. *Crystals* **2017**, *7*, 144. https://doi.org/10.3390/cryst7050144.
31. Tokura, Y.; Okamoto, H.; Koda, T.; Mitani, T.; Saito, G. Pressure-induced neutral-to-ionic phase transition in TTF-*p*-chloranil studied by infrared vibrational spectroscopy. *Solid State Commun.* **1986**, *57*, 607–610.
32. Girlando, A.; Pecile, C.; Brillante, A.; Syassen, K. Neutral-ionic interface in mixed stack charge transfer compounds: Pressure induced ionic phase of tetrathiafulvalene-chloranil (TTF-CA). *Solid State Commun.* **1986**, *57*, 891–896.

33. Horiuchi, S.; Okimoto, Y.; Kumai, R.; Tokura, Y. Anomalous valence fluctuation near a ferroelectric transition in an organic charge-transfer complex. *J. Phys. Soc. Jpn.* **2000**, *69*, 1302–1305. https://doi.org/10.1143/JPSJ.69.1302.
34. Matsuzaki, H.; Takamatsu, H.; Kishida, H.; Okamoto, H. Valence fluctuation and domain-wall dynamics in pressure-induced neutral-to-ionic phase transition of organic charge-transfer crystal. *J. Phys. Soc. Jpn.* **2005**, *74*, 2925–2928. https://doi.org/10.1143/JPSJ.74.2925.
35. Dengl, A.; Beyer, R.; Peterseim, T.; Ivek, T.; Untereiner, G.; Dressel, M. Evolution of ferroelectricity in tetrathiafulvalene-p-chloranil as a function of pressure and temperature. *J. Chem. Phys.* **2014**, *140*, 244511. https://doi.org/10.1063/1.4884964.
36. Lemée-Cailleau, M.H.; Le Cointe, M.; Cailleau, H.; Luty, T.; Moussa, F.; Roos, J.; Brinkmann, D.; Toudic, B.; Ayache, C.; Karl, N. Thermodynamics of the neutral-to-ionic transition as condensation and crystallization of charge-transfer excitations. *Phys. Rev. Lett.* **1997**, *79*, 1690–1693. https://doi.org/10.1103/PhysRevLett.79.1690.
37. Le Cointe, M.; Lemée-Cailleau, M.H.; Cailleau, H.; Toudic, B.; Toupet, L.; Heger, G.; Moussa, F.; Schweiss, P.; Kraft, K.H.; Karl, N. Symmetry breaking and structural changes at the neutral-to-ionic transition in tetrathiafulvalene-*p*-chloranil. *Phys. Rev. B* **1995**, *51*, 3374–3386. https://doi.org/10.1103/PhysRevB.51.3374.
38. Kanai, Y.; Tani, M.; Kagoshima, S.; Tokura, Y.; Koda, T. X-ray evidence for the molecular dimerization in TTF-chloranil. *Synth. Met.* **1984**, *10*, 157–160. https://doi.org/10.1016/0379-6779(84)90091-2.
39. Tokura, Y.; Kaneko, Y.; Okamoto, H.; Tanuma, S.; Koda, T.; Mitani, T.; Saito, G. Spectroscopic study of the neutral-to-ionic phase transition in TTF-Chloranil. *Mol. Cryst. Liq. Cryst.* **1985**, *125*, 71–80. https://doi.org/10.1080/00268948508080088.
40. Kobayashi, K.; Horiuchi, S.; Kumai, R.; Kagawa, F.; Murakami, Y.; Tokura, Y. Electronic ferroelectricity in a molecular crystal with large polarization directing antiparallel to ionic displacement. *Phys. Rev. Lett.* **2012**, *108*, 237601. https://doi.org/10.1103/PhysRevLett.108.237601.
41. Giovannetti, G.; Kumar, S.; Stroppa, A.; Van Den Brink, J.; Picozzi, S. Multiferroicity in TTF-CA organic molecular crystals predicted through Ab initio calculations. *Phys. Rev. Lett.* **2009**, *103*, 266401. https://doi.org/10.1103/PhysRevLett.103.266401.
42. Ishibashi, S.; Terakura, K. Exotic ferroelectricity in tetrathiafulvalene-*p*-chloranil: Anomalous effective charges and a picture in the framework of maximally localized wannier orbitals. *J. Phys. Soc. Jpn.* **2014**, *83*, 073702. https://doi.org/10.7566/JPSJ.83.073702.
43. Borisov, V.; Biswas, S.; Li, Y.; Valentí, R. Microscopic modeling of correlated systems under pressure: Representative examples. *Phys. Status Solidi B* **2019**, *256*, 1900229. https://doi.org/10.1002/pssb.201900229.
44. Resta, R.; Vanderbilt, D. Theory of Polarization: A Modern Approach. In *Physics of Ferroelectrics: A Modern Perspective*; Rabe, K.M., Ahn, C.H., Triscone, J.-M., Eds.; Springer: Berlin/Heidelberg, Germany, 2007; pp. 31–68.
45. King-Smith, R.D.; Vanderbilt, D. Theory of polarization of crystalline solids. *Phys. Rev. B* **1993**, *47*, 1651–1654. https://doi.org/10.1103/PhysRevB.47.1651.
46. Vanderbilt, D.; King-Smith, R.D. Electric polarization as a bulk quantity and its relation to surface charge. *Phys. Rev. B* **1993**, *48*, 4442–4455. https://doi.org/10.1103/PhysRevB.48.4442.
47. Resta, R. Macroscopic polarization in crystalline dielectrics: The geometric phase approach. *Rev. Mod. Phys.* **1994**, *66*, 899–915. https://doi.org/10.1103/RevModPhys.66.899.
48. Nagaosa, N.; Takimoto, J. Theory of neutral-ionic transition in organic crystals. II. Effect of the intersite Coulomb interaction. *J. Phys. Soc. Jpn.* **1986**, *55*, 2745–2753. https://doi.org/10.1143/JPSJ.55.2735.
49. Nagaosa, N. Theory of neutral-ionic transition in organic crystals. IV. Phenomenological viewpoint. *J. Phys. Soc. Jpn.* 1986, *55*, 3488–3497.
50. Kagawa, F.; Horiuchi, S.; Matsui, H.; Kumai, R.; Onose, Y.; Hasegawa, T.; Tokura, Y. Electric-field control of solitons in a ferroelectric organic charge-transfer salt. *Phys. Rev. Lett.* **2010**, *104*, 227602. https://doi.org/10.1103/PhysRevLett.104.227602.
51. Kishida, H.; Takamatsu, H.; Fujinuma, K.; Okamoto, H. Ferroelectric nature and real-space observations of domain motions in the organic charge-transfer compound tetrathiafulvalene-*p*-chloranil. *Phys. Rev. B* **2009**, *80*, 205201. https://doi.org/10.1103/PhysRevB.80.205201.
52. Buron-Le Cointe, M.; Lemée-Cailleau, M.H.; Cailleau, H.; Ravy, S.; Bérar, J.F.; Rouzière, S.; Elkaïm, E.; Collet, E. One-dimensional fluctuating nanodomains in the charge-transfer molecular system TTF-CA and their first-order crystallization. *Phys. Rev. Lett.* **2006**, *96*, 205503. https://doi.org/10.1103/PhysRevLett.96.205503.
53. Morimoto, T.; Miyamoto, T.; Yamakawa, H.; Terashige, T.; Ono, T.; Kida, N.; Okamoto, H. Terahertz-Field-Induced Large Macroscopic Polarization and Domain-Wall Dynamics in an Organic Molecular Dielectric. *Phys. Rev. Lett.* **2017**, *118*, 107602. https://doi.org/10.1103/PhysRevLett.118.107602.
54. Koshihara, S.; Tokura, Y.; Mitani, T.; Saito, G.; Koda, T. Photoinduced valence instability in the organic molecular compound tetrathiafulvalene-*p*-chloranil (TTF-CA). *Phys. Rev. B* **1990**, *42*, 6853.
55. Iwai, S.; Okamoto, H. Ultrafast phase control in one-dimensional correlated electron systems. *J. Phys. Soc. Jpn.* **2006**, *75*, 011007. https://doi.org/10.1143/JPSJ.75.011007.
56. Miyashita, N.; Kuwabara, M.; Yonemitsu, K. Electronic and lattice dynamics in the photoinduced ionic-to-neutral phase transition in a one-dimensional extended Peierls–Hubbard model. *J. Phys. Soc. Jpn.* **2003**, *72*, 2282–2290.
57. Ohmura, S.; Mase, T.; Takahashi, A. Terahertz pulse induced transitions between ionic and neutral phases and electronic polarization reversal in TTF-CA. *Phys. Rev. B* **2019**, *100*, 035116.
58. Watanabe, Y.; Ando, H.; Takahashi, A.; Tomita, N. Nonadiabatic quantum fluctuations in the neutral ground state of tetrathiafulvalene-*p*-chloranil. *Phys. Rev. B* **2019**, *100*, 205205. https://doi.org/10.1103/PhysRevB.100.205205.

59. Miyamoto, T.; Yada, H.; Yamakawa, H.; Okamoto, H. Ultrafast modulation of polarization amplitude by terahertz fields in electronic-type organic ferroelectrics. *Nat. Commun.* **2013**, *4*, 2586. https://doi.org/10.1038/ncomms3586.
60. Takaoka, K.; Kaneko, Y.; Okamoto, H.; Tokura, Y.; Koda, T.; Mitani, T.; Saito, G. Infrared molecular-vibration spectra of tetrathiafulvalene-chloranil crystal at low temperature and high pressure. *Phys. Rev. B* **1987**, *36*, 3884–3887. https://doi.org/10.1103/PhysRevB.36.3884.
61. Luty, T.; Cailleau, H.; Koshihara, S.; Collet, E.; Takesada, M.; Lemée-Cailleau, M.H.; Cointe, M.B.-L.; Nagaosa, N.; Tokura, Y.; Zienkiewicz, E.; et al. Static and dynamic order of cooperative multi-electron transfer. *Europhys. Lett.* **2002**, *59*, 619–625. https://doi.org/10.1209/epl/i2002-00149-4.
62. Metzger, R.M.; Torrance, J.B. Role of the madelung energy in the neutral-ionic phase transition of Tetrathiafulvalene Chloranil. *J. Am. Chem. Soc.* **1985**, *107*, 117–121.
63. Okamoto, H.; Koda, T.; Tokura, Y.; Mitani, T.; Saito, G. Pressure-induced neutral-to-ionic phase transition in organic charge-transfer crystals of tetrathiafulvalene-*p*-benzoquinone derivatives. *Phys. Rev. B* **1989**, *39*, 10693–10701. https://doi.org/10.1103/PhysRevB.39.10693.
64. Masino, M.; Girlando, A.; Brillante, A. Intermediate regime in pressure-induced neutral-ionic transition in tetrathiafulvalene-chloranil. *Phys. Rev. B* **2007**, *76*, 064114. https://doi.org/10.1103/PhysRevB.76.064114.
65. Kishine, J.; Luty, T.; Yonemitsu, K. Ferroelectric phase transition, ionicity condensation, and multicriticality in charge-transfer organic complexes. *Phys. Rev. B* **2004**, *69*, 075115. https://doi.org/10.1103/PhysRevB.69.075115.
66. Gourdji, M.; Guibé, L.; Péneau, A.; Gallier, J.; Toudic, B.; Cailleau, H. ^{35}Cl NQR observation of the neutral-to-ionic phase transition in tetrathiafulvalene-*p*-chloranil. *Solid State Commun.* **1991**, *77*, 609–612.
67. Gallier, J.; Toudic, B.; Delugeard, Y.; Cailleau, H.; Gourdji, M.; Peneau, A.; Guibe, L. Chlorine-nuclear-quadrupole-resonance study of the neutral-to-ionic transition in tetrathiafulvalene-chloranil. *Phys. Rev. B* **1993**, *47*, 11688.
68. Koukoulas, A.A.; Whitehead, M.A. Observations in nuclear quadrupole resonance frequency temperature dependence. *Chem. Phys. Lett.* **1990**, *167*, 379–382. https://doi.org/10.1016/0009-2614(90)85017-7.
69. Yoshinari, Y.; Maniwa, Y.; Takahashi, T.; Mizoguchi, K.; Mitani, T. ^{1}H-NMR studies of neutral-ionic transition in TTF-p-Chloranil. *Synth. Met.* **1987**, *19*, 521–526.
70. Toudic, B.; Gallier, J.; Boumaza, M.; Cailleau, H. Proton spin-lattice relaxation study of the neutral-to-ionic transition in TTF-chloranil. *J. Phys. Fr.* **1990**, *51*, 1671–1678.
71. Barthel, E.; Quiron, G.; Wzietek, P.; Jerome, D.; Christensen, J.; Bechgaard, K. NMR in commensurate and incommensurate spin density waves. *Europhys. Lett.* **1993**, *21*, 87–92. https://doi.org/10.1209/0295-5075/21/1/015.
72. Fujiyama, S.; Nakamura, T. Redistribution of electronic charges in spin-Peierls state in $(TMTTF)_2AsF_6$ observed by ^{13}C NMR. *J. Phys. Soc. Jpn.* **2006**, *75*, 014705. https://doi.org/10.1143/JPSJ.75.014705.
73. Katan, C. First-principles study of the structures and vibrational frequencies for Tetrathiafulvalene TTF and TTF-d_4 in different oxidation states. *J. Phys. Chem. A* **1999**, *103*, 1407–1413. https://doi.org/10.1021/jp983941v.
74. Bonner, J.C.; Fisher, M.E. Linear magnetic chains with anisotropic coupling. *Phys. Rev.* **1964**, *135*, A640. https://doi.org/10.1103/PhysRev.135.A640.
75. Estes, W.E.; Gavel, D.P.; Hatfield, W.E.; Hodgson, D.J. Magnetic and structural characterization of dibromo- and dichlorobis(thiazole)copper(II). *Inorg. Chem.* **1978**, *17*, 1415–1421. https://doi.org/10.1021/ic50184a005.
76. Sachdev, S. NMR relaxation in half-integer antiferromagnetic spin chains. *Phys. Rev. B* **1994**, *50*, 13006–13008. https://doi.org/10.1103/PhysRevB.50.13006.
77. Takigawa, M.; Motoyama, N.; Eisaki, H.; Uchida, S. Dynamics in the $S = 1/2$ one-dimensional antiferromagnet Sr_2CuO_3 via ^{63}Cu NMR. *Phys. Rev. Lett.* **1996**, *76*, 4612–4615. https://doi.org/10.1103/PhysRevLett.76.4612.
78. Devreux, F. Nuclear relaxation in one-dimensional Hubbard systems. *Phys. Rev. B* **1976**, *13*, 4651–4657.
79. Nechtschein, M.; Devreux, F.; Greene, R.L.; Clarke, T.C.; Street, G.B. One-dimensional spin diffusion in polyacetylene, $(CH)_x$. *Phys. Rev. Lett.* **1980**, *44*, 356–359.
80. Mizoguchi, K.; Kume, K.; Shirakawa, H. Frequency dependence of electron spin-lattice relaxation rate at 5-450 MHz in pristine trans-polyacetylene—New evidence of one dimensional diffusive motion of electron spin (neutral soliton) ---. *Solid State Commun.* **1984**, *50*, 213–218. https://doi.org/10.1016/0038-1098(84)90798-1.
81. Devreux, F.; Jeandey, C.; Nechtschein, M.; Fabre, J.M.; Giral, L. Electron-proton couplings and local susceptibilities in TTF and TCNQ salts. *J. Phys.* **1979**, *40*, 671–677.
82. Okamoto, H.; Ishige, Y.; Tanaka, S.; Kishida, H.; Iwai, S.; Tokura, Y. Photoinduced phase transition in tetrathiafulvalene-*p*-chloranil observed in femtosecond reflection spectroscopy. *Phys. Rev. B* **2004**, *70*, 165202. https://doi.org/10.1103/PhysRevB.70.165202.
83. Bruinsma, R.; Per Bak; J.B. Torrance Neutral-ionic transitions in organic mixed-stack compounds. *Phys. Rev. B* **1983**, *27*, 456–466.
84. Karpov, P.; Brazovskii, S. Phase transitions in ensembles of solitons induced by an optical pumping or a strong electric field. *Phys. Rev. B* **2016**, *94*, 125108. https://doi.org/10.1103/PhysRevB.94.125108.
85. Takehara, R.; Miyagawa, K.; Kanoda, K.; Miyamoto, T.; Matsuzaki, H.; Okamoto, H.; Taniguchi, H.; Matsubayashi, K.; Uwatoko, Y. Electron transport in TTF-CA under high pressures. *Physica B* **2015**, *460*, 83–87. https://doi.org/10.1016/j.physb.2014.11.045.
86. Orignac, E.; Chitra, R. Mean-field theory of the spin-Peierls transition. *Phys. Rev. B* **2004**, *70*, 214436. https://doi.org/10.1103/PhysRevB.70.214436.

87. Itoh, Y.; Yasuoka, H. Interrelation between dynamical and static spin gaps in quantum spin systems. *J. Phys. Soc. Jpn.* **1997**, *66*, 334–336.
88. Abragam, A. *The Principles of Nuclear Magnetism*; Oxford University Press: Oxford, UK, 1961.
89. Masino, M.; Girlando, A.; Brillante, A.; Della Valle, R.G.; Venuti, E.; Drichko, N.; Dressel, M. Lattice dynamics of TTF-CA across the neutral-ionic transition. *Chem. Phys.* **2006**, *325*, 71–77. https://doi.org/10.1016/j.chemphys.2005.08.072.